The Astronomical Journal, 167:289 (25pp), 2024 June https://doi.org/10.3847/1538-3881/ad4115

The Discovery and Follow-up of Four Transiting Short-period Sub-Neptunes Orbiting M Dwarfs

Yasunori Hori[1,2,3], Akihiko Fukui[4,5], Teruyuki Hirano[1,2,3], Norio Narita[1,4,5], Jerome P. de Leon[6], Hiroyuki Tako Ishikawa[7], Joel D. Hartman[8], Giuseppe Morello[5,9,10], Nestor Abreu García[5,11], Leticia Álvarez Hernández[5,11], Víctor J. S. Béjar[5,11], Yéssica Calatayud-Borras[5,11], Ilaria Carleo[5,12], Gareb Enoc[5,11], Emma Esparza-Borges[5,11], Izuru Fukuda[6], Daniel Galán[5,11], Samuel Geraldía-González[5,11], Yuya Hayashi[6], Masahiro Ikoma[2,3], Kai Ikuta[6], Keisuke Isogai[6,13], Taiki Kagetani[6], Yugo Kawai[6], Kiyoe Kawauchi[14], Tadahiro Kimura[2], Takanori Kodama[15], Judith Korth[10,16], Nobuhiko Kusakabe[1], Andrés Laza-Ramos[17], John H. Livingston[1,2,3], Rafael Luque[18], Kohei Miyakawa[2], Mayuko Mori[1], Felipe Murgas[5,11], Jaume Orell-Miquel[5,11], Enric Palle[5,11], Hannu Parviainen[5,11], Alberto Peláez-Torres[5,11], Marta Puig-Subirà[5,11], Manuel Sánchez-Benavente[5,11], Paula Sosa-Guillén[5,11], Monika Stangret[19], Yuka Terada[20,21], Sara Muñoz Torres[5], Noriharu Watanabe[6], Gaspar Á. Bakos[8], Khalid Barkaoui[5,22,23], Charles Beichman[24,25], Zouhair Benkhaldoun[26], Andrew W. Boyle[27], David R. Ciardi[27], Catherine A. Clark[24,25], Karen A. Collins[28], Kevin I. Collins[29], Dennis M. Conti[30], Ian J.M. Crossfield[31], Mark E. Everett[32], Elise Furlan[24], Mourad Ghachoui[22,26], Michaël Gillon[22], Erica J. Gonzales[33], Jesus Higuera[32], Keith Horne[34], Steve B. Howell[35], Emmanuël Jehin[36], Kathryn V. Lester[35], Michael B. Lund[24], Rachel Matson[37], Elisabeth C. Matthews[38], Francisco J. Pozuelos[9,22], Boris S. Safonov[39], Joshua E. Schlieder[40], Richard P. Schwarz[28], Ramotholo Sefako[41], Gregor Srdoc[42], Ivan A. Strakhov[39], Mathilde Timmermans[22], William C. Waalkes[43], Carl Ziegler[44], David Charbonneau[28], Zahra Essack[45], Natalia M. Guerrero[46,47], Hiroki Harakawa[48], Christina Hedges[40], Masato Ishizuka[49], Jon M. Jenkins[35], Mihoko Konishi[50], Takayuki Kotani[1,2,3], Tomoyuki Kudo[48], Takashi Kurokawa[2,51], Masayuki Kuzuhara[1,2], Jun Nishikawa[1,2,3], Masashi Omiya[1,2], George R. Ricker[46], Sara Seager[46,52,53], Takuma Serizawa[2,51], Stephanie Striegel[54], Motohide Tamura[1,2,49], Akitoshi Ueda[1,2,3], Roland Vanderspek[46], Sébastien Vievard[48], and Joshua N. Winn[8]

[1] Astrobiology Center, 2-21-1 Osawa, Mitaka, Tokyo 181-8588, Japan; yasunori.hori@nao.ac.jp
[2] National Astronomical Observatory of Japan, 2-21-1 Osawa, Mitaka, Tokyo 181-8588, Japan
[3] Department of Astronomical Science, The Graduated University for Advanced Studies (SOKENDAI), 2-21-1 Osawa, Mitaka, Tokyo 181-8588, Japan
[4] Komaba Institute for Science, The University of Tokyo, 3-8-1 Komaba, Meguro, Tokyo 153-8902, Japan
[5] Instituto de Astrofísica de Canarias (IAC), E-38200 La Laguna, Tenerife, Spain
[6] Department of Multi-Disciplinary Sciences, Graduate School of Arts and Sciences, The University of Tokyo, 3-8-1 Komaba, Meguro, Tokyo 153-8902, Japan
[7] Department of Physics and Astronomy, The University of Western Ontario, 1151 Richmond Street, London, ON N6A 3K7, Canada
[8] Department of Astrophysical Sciences, Princeton University, NJ 08544, USA
[9] Instituto de Astrofísica de Andalucía (IAA-CSIC), Glorieta de la Astronomía s/n, 18008 Granada, Spain
[10] Department of Space, Earth and Environment, Chalmers University of Technology, SE-412 96 Gothenburg, Sweden
[11] Departamento de Astrofísica, Universidad de La Laguna (ULL), E-38206 La Laguna, Tenerife, Spain
[12] INAF—Osservatorio Astrofisico di Torino, Via Osservatorio 20, I-10025, Pino Torinese, Italy
[13] Okayama Observatory, Kyoto University, 3037-5 Honjo, Kamogatacho, Asakuchi, Okayama 719-0232, Japan
[14] Department of Physical Sciences, Ritsumeikan University, 1-1-1 Nojihigashi, Kusatsu, Shiga 525-8577, Japan
[15] Earth-Life Science Institute (ELSI), Tokyo Institute of Technology, 2-12-1-I7E-315 Ookayama, Meguro-ku, Tokyo 152-8550, Japan
[16] Lund Observatory, Division of Astrophysics, Department of Physics, Lund University, Box 43, 22100 Lund, Sweden
[17] Departamento de Astronomía y Astrofísica, Universidad de Valencia (UV), E-46100, Burjassot, Valencia, Spain
[18] Department of Astronomy & Astrophysics, University of Chicago, Chicago, IL 60637, USA
[19] INAF—Osservatorio Astronomico di Padova, Vicolo dell'Osservatorio 5, 35122 Padova, Italy
[20] Institute of Astronomy and Astrophysics, Academia Sinica, P.O. Box 23-141, Taipei 10617, Taiwan, R.O.C.
[21] Department of Astrophysics, National Taiwan University, Taipei 10617, Taiwan, R.O.C.
[22] Astrobiology Research Unit, Université de Liège, 19C Allée du 6 Août, 4000 Liège, Belgium
[23] Department of Earth, Atmospheric and Planetary Science, Massachusetts Institute of Technology, Cambridge, MA 02139, USA
[24] NASA Exoplanet Science Institute—Caltech/IPAC, 1200 E. California Boulevard, Pasadena, CA 91125, USA
[25] Jet Propulsion Laboratory, California Institute of Technology, Pasadena, CA 91109, USA
[26] Oukaimeden Observatory, High Energy Physics and Astrophysics Laboratory, Faculty of sciences Semlalia, Cadi Ayyad University, Marrakech, Morocco
[27] Department of Astronomy, California Institute of Technology, 1200 E. California Boulevard, Pasadena, CA 91125, USA
[28] Center for Astrophysics | Harvard & Smithsonian, 60 Garden Street, Cambridge, MA 02138, USA
[29] George Mason University, 4400 University Drive, Fairfax, VA 22030, USA
[30] American Association of Variable Star Observers, 185 Alewife Brook Parkway, Suite 410, Cambridge, MA 02138, USA
[31] Department of Physics & Astronomy, University of Kansas, KS 66045, USA
[32] NSF's National Optical-Infrared Astronomy Research Laboratory, 950 N. Cherry Avenue, Tucson, AZ 85719, USA
[33] Department of Astronomy and Astrophysics, University of California, Santa Cruz, CA 95064, USA
[34] SUPA Physics and Astronomy, University of St. Andrews, Fife, KY16 9SS Scotland, UK
[35] NASA Ames Research Center, Moffett Field, CA 94035, USA
[36] Space Sciences, Technologies and Astrophysics Research (STAR) Institute, Université de Liège, Allée du 6 Août 19C, B-4000 Liège, Belgium
[37] U.S. Naval Observatory, Washington, D.C. 20392, USA
[38] Max-Planck-Institut für Astronomie, Königstuhl 17, 69117 Heidelberg, Germany
[39] Sternberg Astronomical Institute, Lomonosov Moscow State University, 119992, Universitetskii prospekt 13, Moscow, Russia
[40] NASA Goddard Space Flight Center, 8800 Greenbelt Road, Greenbelt, MD 20771, USA
[41] South African Astronomical Observatory, P.O. Box 9, Observatory, Cape Town 7935, South Africa
[42] Kotizarovci Observatory, Sarsoni 90, 51216 Viskovo, Croatia

[43] Department of Astrophysical and Planetary Sciences, University of Colorado, Boulder, CO 80309, USA
[44] Department of Physics, Engineering and Astronomy, Stephen F. Austin State University, 1936 North Street, Nacogdoches, TX 75962, USA
[45] Department of Physics and Astronomy, University of New Mexico, 210 Yale Boulevard NE, Albuquerque, NM 87106, USA
[46] Department of Physics and Kavli Institute for Astrophysics and Space Research, Massachusetts Institute of Technology, 77 Massachusetts Avenue, Cambridge, MA 02139, USA
[47] Department of Astronomy, University of Florida, Gainesville, FL 32611, USA
[48] Subaru Telescope, 650 N. Aohoku Place, Hilo, HI 96720, USA
[49] Department of Astronomy, Graduate School of Sciences, The University of Tokyo, 7-3-1 Hongo, Bunkyo-ku, Tokyo 113-0033, Japan
[50] Faculty of Science and Technology, Oita University, 700 Dannoharu, Oita 870-1192, Japan
[51] Institute of Engineering, Tokyo University of Agriculture and Technology, 2-24-26 Nakacho, Koganei, Tokyo 184-8588, Japan
[52] Department of Earth, Atmospheric and Planetary Sciences, Massachusetts Institute of Technology, 77 Massachusetts Avenue, Cambridge, MA 02139, USA
[53] Department of Aeronautics and Astronautics, Massachusetts Institute of Technology, 77 Massachusetts Avenue, Cambridge, MA 02139, USA
[54] SETI Institute, Mountain View, CA 94043, USA
Received 2023 September 25; revised 2024 March 26; accepted 2024 April 18; published 2024 May 30

Abstract

Sub-Neptunes with radii of 2–3 $R_\oplus$ are intermediate in size between rocky planets and Neptune-sized planets. The orbital properties and bulk compositions of transiting sub-Neptunes provide clues to the formation and evolution of close-in small planets. In this paper, we present the discovery and follow-up of four sub-Neptunes orbiting M dwarfs (TOI-782, TOI-1448, TOI-2120, and TOI-2406), three of which were newly validated by ground-based follow-up observations and statistical analyses. TOI-782 b, TOI-1448 b, TOI-2120 b, and TOI-2406 b have radii of $R_p = 2.740^{+0.082}_{-0.079}\ R_\oplus$, $2.769^{+0.073}_{-0.068}\ R_\oplus$, $2.120 \pm 0.067\ R_\oplus$, and $2.830^{+0.068}_{-0.066}\ R_\oplus$ and orbital periods of $P = 8.02$, 8.11, 5.80, and 3.08 days, respectively. Doppler monitoring with the Subaru/InfraRed Doppler instrument led to 2σ upper limits on the masses of $<19.1\ M_\oplus$, $<19.5\ M_\oplus$, $<6.8\ M_\oplus$, and $<15.6\ M_\oplus$ for TOI-782 b, TOI-1448 b, TOI-2120 b, and TOI-2406 b, respectively. The mass–radius relationship of these four sub-Neptunes testifies to the existence of volatile material in their interiors. These four sub-Neptunes, which are located above the so-called "radius valley," are likely to retain a significant atmosphere and/or an icy mantle on the core, such as a water world. We find that at least three of the four sub-Neptunes (TOI-782 b, TOI-2120 b, and TOI-2406 b), orbiting M dwarfs older than 1 Gyr, are likely to have eccentricities of $e \sim 0.2$–0.3. The fact that tidal circularization of their orbits is not achieved over 1 Gyr suggests inefficient tidal dissipation in their interiors.

Unified Astronomy Thesaurus concepts: Exoplanets (498); Mini Neptunes (1063); Radial velocity (1332); Transit photometry (1709); Tides (1702); M dwarf stars (982)

Supporting material: machine-readable table

1. Introduction

About 70%–80% of stars in the solar neighborhood are M dwarfs (e.g., Winters et al. 2019, 2021). Nearby M dwarfs are suitable targets to search for low-mass planets. Recent discoveries of temperate planets orbiting nearby M dwarfs, such as TRAPPIST-1 (Gillon et al. 2017), provide a unique opportunity for atmospheric characterization of terrestrial planets beyond the solar system. Near-infrared spectrographs designed for high-precision radial velocity (RV) measurements, such as the Very Large Telescope/CRIRES+ (Dorn et al. 2016), the Hobby–Eberly Telescope/Habitable Zone Planet Finder (Mahadevan et al. 2018), Subaru/InfraRed Doppler (IRD; Kotani et al. 2018), CARMENES (Quirrenbach et al. 2014), PARVI (Gibson et al. 2020), NIRPS (Wildi et al. 2017), CFHT/SPIRou (Donati et al. 2020), and Gemini/MAROON-X (Seifahrt et al. 2018), have begun to find planets down to an Earth mass around M dwarfs, such as Teegarden's Star (Zechmeister et al. 2019). Also, space-based planet surveys have accelerated the detection of planets orbiting M dwarfs. The successor to Kepler, the Transiting Exoplanets Survey Satellite (TESS), which launched in 2018, has conducted the first-ever all-sky photometric survey for planets around bright stars (Ricker et al. 2015). The TESS bandpass spanning from 600 to 1000 nm is well suited for detecting planets around cool stars. About one-fourth of confirmed TESS planets have been discovered around cool stars (Guerrero et al. 2021).

Both transit detection (Dressing & Charbonneau 2013, 2015; Mulders et al. 2015; Hsu et al. 2020) and RV surveys (Bonfils et al. 2013; Tuomi et al. 2014; Maldonado et al. 2020; Sabotta et al. 2021) revealed that small planets are ubiquitous around cool stars. There is a deficit of planets with radii ~ 1.5–2 $R_\oplus$, which is called the "radius valley," in the planet population observed around FGK-type stars (Fulton & Petigura 2018; Van Eylen et al. 2018; Martinez et al. 2019; Berger et al. 2020; Petigura et al. 2022). Also, small planets have a bimodal radius valley distribution in the occurrence rate of planets around M dwarfs (Hirano et al. 2018; Hardegree-Ullman et al. 2019; Cloutier & Menou 2020). The radius valley is interpreted as the compositional transition between bare rocky planets and planets with significant atmospheres (Weiss & Marcy 2014; Rogers 2015). It should be noted that close-in planets ($P < 100$ days) with radii of 2–4 $R_\oplus$ above the radius valley (hereafter, sub-Neptunes) outnumber larger planets, such as Neptune- and Jupiter-sized planets (e.g., Sandoval et al. 2021; Bergsten et al. 2022).

The measured densities of almost all of sub-Neptunes are too low to be consistent with pure rock and metal, and thereby suggest a large mass fraction of volatile material. Many sub-Neptunes with densities lower than those of planets composed of pure H_2O retain atmospheres up to the present day. The atmospheres of planets in the proximity of a central star reflect the competing processes of the accumulation of the disk gas (e.g., Ikoma & Hori 2012; Lee et al. 2014; Ormel et al. 2015;

Kurokawa & Tanigawa 2018; Kuwahara et al. 2019) and secondary gases, as well as atmospheric escape by photoevaporation (e.g., Lopez & Fortney 2013; Owen & Wu 2013, 2017) and core-powered mass loss (Ginzburg et al. 2016, 2018; Gupta & Schlichting 2019; Gupta et al. 2022). Understanding the prevalence of sub-Neptunes with significant atmospheres helps to disentangle the accretion histories of low-mass planets.

We report four sub-Neptunes orbiting M dwarfs from TESS (TOI-782 b, TOI-1448 b, TOI-2120 b, and TOI-2406 b) validated by ground-based follow-up observations using multicolor photometry, high-resolution imaging, and Subaru/IRD RV measurements and statistical analyses, three of which are newly confirmed by this study; the discovery of TOI-2406 b was first reported in Wells et al. (2021). We also obtain their (upper limit) masses at the 2σ confidence level from high-precision RV measurements using Subaru/IRD. We find that at least three sub-Neptunes around a mature M dwarf with age $\gtrsim 1$ Gyr are likely to have eccentricities of $e \sim 0.2$–0.3. Such a nonzero eccentricity of a short-period planet invokes inefficient tidal dissipation in the interior (e.g., Wang & Ford 2011).

This paper is structured as follows. We describe the TESS photometry and our ground-based follow-up observations in Section 2. We present data analyses and the properties of the four M dwarfs and their planets in Section 3. In Section 4, we discuss the interior structures of short-period sub-Neptunes with nonzero eccentricities. In the last section, Section 5, we summarize our results.

2. Observations

2.1. TESS Photometry

TOI-782 (TIC 429358906), TOI-1448 (TIC 343628284), TOI-2120 (TIC 389900760), and TOI-2406 (TIC 212957629) were observed by TESS in three (Sectors 10, 36, and 63), four (Sectors 15, 16, 17, and 57), five (Sectors 18, 24, 25, 52, and 58), and five (Sectors 3, 30, 42, 43, and 70) sectors, respectively. All of these stars were recorded in postage stamps with a cadence of 2 minutes, except for TOI-1448 in Sector 17 and TOI-2406 in Sector 3 for which only the full-frame images (FFIs) stacked with a cadence of 30 minutes are available. The data were processed using a pipeline developed by the Science Processing Operations Center (SPOC) at the NASA Ames Research Center (Jenkins et al. 2016), from which transit signals with periods of 8.02, 8.11, 5.80, and 3.08 days were detected in the light curves of TOI-782, TOI-1448, TOI-2120, and TOI-2406, respectively, using dedicated pipelines (Jenkins et al. 2010; Twicken et al. 2018). The transit signatures passed all the diagnostic tests presented in the Data Validation reports, including the odd/even transit depth test, the weak secondary eclipse test, the ghost diagnostic test, the statistical bootstrap test, the period coincidence test with additional transit-like signals, and the difference image centroiding test for the offset from the Tess Input Catalog (TIC) position of the host star. According to the difference image centroiding tests, the host star is located within $6\farcs0 \pm 3\farcs0$, $3\farcs6 \pm 4\farcs2$, $0\farcs7 \pm 3\farcs4$, and $1\farcs6 \pm 3\farcs1$ of the transit signal sources of TOI-782, TOI-1448, TOI-2120, and TOI-2406, respectively. These planetary candidates were released as TESS Objects of Interests (TOIs) 782.01, 1448.01, 2120.01, and 2406.01 by the TESS Science Office at the Massachusetts Institute of Technology (Guerrero et al. 2021) on UT 2019 June 11, 2019 November 14, 2020 July 19, and 2020 November 24, respectively. Wells et al. (2021) validated the planetary nature of TOI-2406.01, which is now referred to as TOI-2406 b. In this paper, we validate the planetary nature of the rest, TOI-782.01, TOI-1448.01, and TOI-2120.01, which are hereafter referred to as TOI-782 b, TOI-1448 b, and TOI-2120 b, respectively.

For further analyses, we downloaded the Presearch Data Conditioning Simple Aperture Photometry (PDC-SAP; Smith et al. 2012; Stumpe et al. 2012, 2014) where available, otherwise, the TESS-SPOC light curves that are extracted from the FFIs (Caldwell et al. 2020) in the Mikulski Archive for Space Telescopes at the Space Telescope Science Institute. The light curves were normalized to unity sector by sector after removing data points with bad-quality flags.

2.2. Multicolor Transit Photometry from the Ground

We conducted multiband transit photometry of TOI-782 b, TOI-1448 b, TOI-2120 b, and TOI-2406 b from the ground as part of the TESS Follow-up Observing Program (TFOP; Collins 2019)[55] to confirm the transit signals detected by TESS. We checked for chromaticity in the transit depths, that is, a sign of false positives due to contamination from eclipsing binaries (EBs) and refined the physical parameters of the planetary candidates. We utilized a customized version of the `Tapir` software package (Jensen 2013), the `TESS Transit Finder`, to schedule our transit observations. All the observations that are used in our analyses are summarized in Table 1.

Below we briefly describe the observations and data reductions conducted at each facility.

2.2.1. TCS 1.52 m/MuSCAT2

We observed one transit of TOI-782.01 and one transit of TOI-1448 b with the multiband imager MuSCAT2 (Narita et al. 2019), which is mounted on the 1.52 m Telescopio Carlos Sánchez (TCS) telescope at the Teide Observatory in the Canary Islands, Spain. MuSCAT2 has four optical channels each equipped with a $1\mathrm{k} \times 1\mathrm{k}$ CCD camera with a pixel scale of $0\farcs44$ pixel^{-1}, providing a field of view (FOV) of $7\farcm4 \times 7\farcm4$, and is capable of simultaneous imaging in the g, r, i, and z_s bands. The exposure times were set independently for each band as shown in Table 1. The airmass range and the median FWHM of the stellar point-spread function in each band of each observation are also given in Table 1. We performed image calibration and aperture photometry to extract relative light curves using the pipeline described in Fukui et al. (2011).

2.2.2. FTN 2 m/MuSCAT3

We observed one transit of TOI-782 b, one transit of TOI-1448 b, three transits of TOI-2120 b, and one transit of TOI-2406 b with the multiband imager MuSCAT3 (Narita et al. 2020), which is mounted on the 2 m Faulkes Telescope North (FTN), owned and operated by the Las Cumbres Observatory (LCO), located at the Haleakala Observatory in Hawaii, USA. As with MuSCAT2, MuSCAT3 is capable of simultaneous imaging in the g, r, i, and z_s bands, but is equipped with a $2\mathrm{k} \times 2\mathrm{k}$ CCD camera with a pixel scale of $0\farcs27$ pixels^{-1}, providing an FOV of $9\farcm1 \times 9\farcm1$ at each channel. The exposure

[55] https://tess.mit.edu/followup

Table 1
Observation Log of Transit Photometry from the Ground

Planet	Date (UT)	Telescope/Site	Instrument	Filter(s)	Exp. times (s)	FWHM[a] (″)	Airmass (start–min–end)
TOI-782 b	2020 Mar 21	LCO 1 m/SSO	Sinistro	i	60	2.2	2.00–1.02–1.51
TOI-782 b	2021 Feb 21	LCO 1 m/SSO	Sinistro	g	270	1.6	1.54–1.02–1.02
TOI-782 b	2021 Mar 9	LCO 1 m/SSO	Sinistro	z_s	125	1.8	1.12–1.02–1.19
TOI-782 b	2021 May 12	LCO 1 m/SAAO	Sinistro	g	300	2.1	1.09–1.03–1.26
TOI-782 b	2021 Jul 15	LCO 1 m/CTIO	Sinistro	g	300	2.3	1.10–2.04
TOI-782 b	2022 Jan 8	FTN 2 m/Haleakala	MuSCAT3	g, r, i, z_s	60, 30, 21, 18	2.9, 3.1, 3.1, 3.1	2.25–1.30–1.30
TOI-782 b	2022 Apr 30	LCO 1 m/SAAO	Sinistro	z_s	120	1.9	1.06–1.03–1.41
TOI-782 b	2022 Apr 30	TCS 1.52 m/Teide	MuSCAT2	g, r, i, z_s	30, 30, 15, 15	3.0, 3.0, 2.6, 2.6	1.76–1.47–1.51
TOI-1448 b	2020 Jun 20	TCS 1.52 m/Teide	MuSCAT2	g, r, i, z_s	120, 60, 20, 15	3.0, 2.6, 2.2, 2.1	1.55–1.15–1.16
TOI-1448 b	2021 Jul 15	FTN 2 m/Haleakala	MuSCAT3	g, r, i, z_s	55, 35, 25, 20	1.5, 1.3, 1.3, 1.2	1.69–1.25–1.41
TOI-1448 b	2021 Aug 24	LCO 1 m/Teide	Sinistro	i	150	1.9	1.45–1.15–1.70
TOI-2120 b	2020 Jan 21	LCO 1 m/McDonald	Sinistro	I_c	60	2.4	1.26–1.22–1.33
TOI-2120 b	2021 Jan 16	FTN 2 m/Haleakala	MuSCAT3	g, r, i, z_s	300, 88, 40, 26	2.6, 2.2, 1.7, 1.3	1.47–2.13
TOI-2120 b	2021 Jul 14	TRAPPIST-North/Oukaïmeden	Andor iKon-L	z	70	3.4	2.32–1.29
TOI-2120 b	2021 Aug 1	FTN 2 m/Haleakala	MuSCAT3	g, r, i, z_s	300, 88, 40, 17	3.1, 2.8, 2.7, 2.3	2.28–1.49
TOI-2120 b	2022 Jan 28	FTN 2 m/Haleakala	MuSCAT3	g, r, i, z_s	60, 30, 22, 14	3.0, 3.1, 3.2, 3.0	1.48–2.09
TOI-2406 b	2021 Aug 12	FTN 2 m/Haleakala	MuSCAT3	g, r, i, z_s	250, 183, 120, 70	2.1, 2.1, 2.2, 1.9	1.82–1.10–1.13

Note. Key: Siding Spring Observatory (SSO),
[a] Median or typical value during the observation is shown.

times, the median FWHM values, and the airmass range for each observation are reported in Table 1. We performed image calibration and aperture photometry on the obtained images in the same way as for the MuSCAT2 data.

2.2.3. LCO 1 m/Sinistro

We observed six transits of TOI-782 b, one transit of TOI-1448 b, and one transit of TOI-2120 b using the Las Cumbres Observatory Global Telescope (LCOGT; Brown et al. 2013) 1.0 m telescope network. The telescopes are equipped with 4096×4096 Sinistro cameras having an image scale of 0.″389 per pixel, resulting in an FOV of $26' \times 26'$. The exposure times, the typical FWHM values, and the airmass range for each observation are given in Table 1. The images were calibrated using the standard LCOGT `BANZAI` pipeline (McCully et al. 2018) and differential photometric data were extracted using `AstroImageJ` (Collins et al. 2017).

2.2.4. TRAPPIST-North

We observed one full transit of TOI-2120 b with the 0.6 m TRAPPIST-North telescope located at the Oukaimeden Observatory in Morocco (Jehin et al. 2011; Gillon et al. 2013; Barkaoui et al. 2019) on UT 2021 July 14. TRAPPIST-North is equipped with a thermoelectrically cooled $2k \times 2k$ Andor iKon-L BEX2-DD CCD camera with a pixel scale of 0.″64, offering an FOV of $20' \times 20'$. We collected 186 images in the Sloan z' band with an exposure time of 70 s. The typical FWHM values and airmass range for this observation are shown in Table 1. We performed data reduction and differential aperture photometry using `prose`[56] (Garcia et al. 2022), which automatically selected the optimum apertures for the photometric data extraction to be 5.05 pixels (3.″23).

[56] https://github.com/lgrcia/prose

2.3. High-dispersion Spectroscopy with Subaru/IRD

We obtained time series of high-resolution spectra of TOI-782, TOI-1448, TOI-2120, and TOI-2406 with the IRD instrument on the 8.2 m Subaru telescope (Tamura et al. 2012; Kotani et al. 2018) between UT 2019 June 17 and 2022 October 10, as part of the Subaru/IRD TESS intensive follow-up program (ID: S20B-088I). The IRD is a fiber-fed spectrograph covering near-infrared wavelengths from 930 nm to 1740 nm with a spectral resolution of ≈70,000. The integration time per exposure was set to 600–1200 s depending on the stellar brightness and observing conditions on each night. In total, we obtained 25, 21, 24, and 22 exposures for TOI-782, TOI-1448, TOI-2120, and TOI-2406, respectively. We also observed at least one telluric standard star (A0 or A1 star) on each night to correct the telluric lines when extracting the template spectrum for the RV analysis.

The raw IRD data were reduced by the procedure described in Kuzuhara et al. (2018) and Hirano et al. (2020), where the wavelengths were calibrated by spectra from a laser-frequency comb. The reduced one-dimensional spectra have typical signal-to-noise ratios (S/Ns) of 30–60 pixel^{-1} at 1000 nm, except for TOI-2406, whose S/N was 13–28 due to its faintness. We discarded data with S/Ns lower than 18, which could be affected by detector persistence. We also discarded the data that are logged as being affected by passing clouds or instrumental troubles (e.g., guiding errors) during the exposures, leaving 24, 16, 17, and 11 spectra for TOI-782, TOI-1448, TOI-2120, and TOI-2406, respectively. The RVs for each target were extracted following the procedure of Hirano et al. (2020) using the forward modeling technique: for each target, the RV-analysis pipeline derives a telluric-free template spectrum of the target, which is used to model and fit the individual observed spectra taking into account the instantaneous variations in the instrumental profiles. The measured RV

Table 2
Radial Velocities of the Host Stars Measured with Subaru/IRD

Name	Time (BJD_{TDB})	RV ($m\ s^{-1}$)	σ_{RV} ($m\ s^{-1}$)	S/N[a]
TOI-782	2458651.807498	1.28	5.29	37.5
TOI-782	2458651.814354	−10.92	5.77	33.3
TOI-782	2458652.796944	0.07	5.46	37.0
TOI-782	2458652.804249	3.24	5.77	34.7
TOI-782	2458652.811564	4.3	5.55	35.9

Note. Only a portion of this table is shown here to demonstrate its form and content. A machine-readable version of the full table is available.
[a] Measured at the wavelength of 1000 nm.

(This table is available in its entirety in machine-readable form.)

values and 1σ uncertainties along with the S/N ratios at 1000 nm of the original spectra are reported in Table 2. The median RV internal errors are 5.3, 5.7, 4.6, and 14.5 $m\ s^{-1}$ for TOI-782, TOI-1448, TOI-2120, and TOI-2406, respectively. The RV uncertainties vary slightly from frame to frame, reflecting the sky conditions and resulting S/N ratio for each frame. About half of the spectra were obtained under good observing conditions, in which case we achieved the expected S/N ratios and RV internal errors.

2.4. High-resolution Imaging

To investigate whether there are companion or background stars close to the host stars, we obtained adaptive optics (AO) and speckle images of TOI-782, TOI-1448, and TOI-2120 with various facilities as part of TFOP. The observational dates, instruments, filters, and achieved contrasts are summarized in Table 3. The observations for individual targets are briefly described below.

2.4.1. TOI-782

We conducted AO observations of TOI-782 with the NIRC2 instrument on Keck II behind the natural guide star AO system (Wizinowich et al. 2000) on UT 2019 June 25 with the J_{cont} ($\lambda_0 = 1.213\ \mu m$, $\Delta\lambda = 0.019\ \mu m$) and Br$\gamma$ ($\lambda_0 = 2.168\ \mu m$, $\Delta\lambda = 0.033\ \mu m$) band filters, and with NIRI (Hodapp et al. 2003) on the 8.2 m Gemini-N telescope on the same night with the Brγ ($\lambda_0 = 2.1686\ \mu m$, $\Delta\lambda = 0.0294\ \mu m$) filter. We also conducted speckle imaging observations with HRCam (Tokovinin et al. 2010) on the 4.1 m SOAR telescope on UT 2019 July 14 with the Cousins *I*-band filter, and used data from the Differential Speckle Survey Instrument (DSSI; Horch et al. 2009) on the Lowell Discovery Telescope (LDT) from UT 2020 February 9 using narrowband filters with center wavelengths of 692 nm ($\Delta\lambda = 40$ nm) and 880 nm ($\Delta\lambda = 50$ nm), as reported in Clark et al. (2022). We achieved a 5σ contrast at a separation of 0.″5 of up to 7.7 mag. We did not detect a nearby star within 2″ in any of the observations.

2.4.2. TOI-1448

We conducted AO observations of TOI-1448 with PHARO (Hayward et al. 2001) behind the natural guide star AO system P3K (Dekany et al. 2013) of the Palomar 5 m telescope on UT 2021 August 24 with a Brγ-band ($\lambda_0 = 2.1686\ \mu m$, $\Delta\lambda = 0.0326\ \mu m$) filter. We also conducted speckle imaging observations with NESSI (Scott et al. 2018) on the WIYN 3.5 m telescope on UT 2022 September 17 using narrowband filters with central wavelengths of 562 nm ($\Delta\lambda = 44$ nm) and 832 nm ($\Delta\lambda = 40$ nm). We achieved a 5σ contrast at 0.″5 of up to 7.7 mag. We did not detect a nearby star within 2″ in any of the observations.

2.4.3. TOI-2120

We conducted speckle imaging observations with Speckle Polarimeter (Safonov et al. 2017) on the SAI-2.5 m telescope on UT 2020 October 27 in the *I* band, and with 'Alopeke[57] (Scott et al. 2021) on the Gemini-N telescope on UT 2020 December 3 with the 562 nm ($\Delta\lambda = 54$ nm) and 832 nm ($\Delta\lambda = 40$ nm) band filters. We achieved a 5σ contrast at 0.″5 of up to 5.6 mag. We did not detect a nearby star within 2″ in any of the observations.

3. Data Analysis and Results

3.1. Properties of the Host Stars

3.1.1. Spectroscopic Properties

We estimated the metallicity ([Fe/H]) and the effective temperature (T_{eff}) of four host stars using the IRD spectra following the procedure described in Mori et al. (2022). For TOI-782 b, TOI-1448 b, and TOI- 2120 b, we used the template spectra identical to those used for the RV analysis, but for TOI-2406 b, we used a combined spectrum before deconvolving the instrument profile to avoid amplifying the additional noise due to the low S/N. The basic concept of our analysis is an equivalent width (EW) comparison of individual atomic and molecular absorption lines between the synthetic and observed spectra. To determine the T_{eff} value, 47 FeH molecular lines at 990–1012 nm were used (see Ishikawa et al. 2022 for details). We employed a total of 25 atomic lines corresponding to Na I, Mg I, Ca I, Ti I, Cr I, Mn I, Fe I, and Sr II as a measure of the elemental abundances (Ishikawa et al. 2020). We selected only atomic lines with a high S/N. We obtained the EWs of the atomic lines by fitting the synthetic spectra line by line, while the EWs of the FeH lines were obtained from a Gaussian fitting to each line. The logarithm of the surface gravity $\log g$ and the microturbulent velocity were fixed at 5.0 and 0.5 $km\ s^{-1}$, respectively, for all the targets. We checked that this assumption causes a negligible change in the final T_{eff} and [Fe/H] estimates.

First, we derived T_{eff} from the EWs of the FeH lines, assuming solar abundances. Subsequently, we determined the individual abundances of the eight elements, i.e., [X/H], using the T_{eff} value. Then, we carried out these analyses for [X/H] and T_{eff} in an iterative process until the T_{eff} and [Fe/H] matched the values assumed in the previous iteration step within their uncertainties. We obtained $[Fe/H] = 0.34 \pm 0.15$, 0.37 ± 0.14, 0.39 ± 0.22, and -0.26 ± 0.24 dex, and $T_{eff} = 3379 \pm 100$ K, 3390 ± 100 K, 3183 ± 100 K, and 3308 ± 100 K for TOI-782, TOI-1448, TOI-2120, and TOI-2406, respectively. Note that our [Fe/H] value for TOI-2406 is consistent with that derived by Wells et al. (2021) within the uncertainties.

Using the IRD spectra, we also derived the systemic RVs of our targets. We fitted Gaussian functions to relatively deep atomic lines (30–40 lines) at near-infrared wavelengths and compared the line centers with their vacuum wavelengths. The

[57] https://www.gemini.edu/sciops/instruments/alopeke-zorro/

Table 3
Observation Log of High-contrast Imaging

Star	Date (UT)	Telescope	Instrument	Filter(s)	Image type	Contrast at 0.″5 (Δmag)
TOI-782	2019 Jun 25	Keck II	NIRC2	J_{cont}, Brγ	AO	7.1, 7.7
TOI-782	2019 Jun 25	Gemini-N	NIRI	Brγ	AO	5.6
TOI-782	2019 Jul 14	SOAR	HRCam	I	Speckle	4.5
TOI-782	2020 Feb 9	LDT	DSSI	692 nm, 880 nm	Speckle	4.2, 4.6
TOI-1448	2021 Aug 24	Palomar 5 m	PHARO	Brγ	AO	7.0
TOI-1448	2022 Sep 17	WIYN	NESSI	562 nm, 832 nm	Speckle	4.2, 4.0
TOI-2120	2020 Oct 27	SAI[1] 2.5 m	Speckle Polarimeter	I	Speckle	3.8
TOI-2120	2020 Dec 3	Gemini-N	'Alopeke	562 nm, 832 nm	Speckle	4.3, 5.6
TOI-2406	2020 Dec 29	Gemini-S	Zorro	562 nm, 832 nm	Speckle	4.1, 4.9
TOI-2406	2021 Sep 19	Gemini-S	Zorro	562 nm, 832 nm	Speckle	4.6, 5.3
TOI-2406	2021 Sep 19	Palomar 5 m	PHARO	BrG	AO	5.8

[1] Sternberg Astronomical Institute

systemic RVs and their uncertainties were then derived from the mean values and the scatter of the measurements as listed in Table 4. Inputting the systemic RVs together with the coordinates, parallaxes, and proper motions, we computed the Galactic space velocities (U, V, W) for the four stars using the Python script `uvw_errs` (Rodriguez 2016). The derived UVW velocities are also listed in Table 4. For all of our targets, we found that the sky-projected rotational velocity ($v \sin i_s$) of each star is too small (smaller than the spectral resolution, or ∼4.3 km s^{-1}) to detect from IRD spectra in a well-calibrated way.

3.1.2. Photometric Properties

We estimated the stellar parameters other than [Fe/H] mainly from the photometric magnitudes as follows. First, we estimated the stellar radius (R_s) and mass (M_s) through the empirical luminosity–metallicity–radius and luminosity–metallicity–mass relations of Mann et al. (2015) and Mann et al. (2019), respectively, adopting the parallaxes from Gaia DR3 (Gaia Collaboration et al. 2016, 2023; assuming the distance d is the inverse of the parallax), the K_s-band magnitudes from the Two Micron All Sky Survey (2MASS; Skrutskie et al. 2006), and the [Fe/H] values derived in Section 3.1.1. The stellar radii were estimated to be 0.398 ± 0.012 $R_\odot$, 0.376 ± 0.011 $R_\odot$, 0.237 ± 0.007 $R_\odot$, and 0.201 ± 0.006 $R_\odot$ for TOI-782, TOI-1448, TOI-2120, and TOI-2406, respectively. These values were used as priors in the spectral energy distribution (SED) fitting as described below. The stellar masses were estimated to be 0.397 ± 0.010 $M_\odot$, 0.372 ± 0.009 $M_\odot$, 0.211 ± 0.005 $M_\odot$, and 0.166 ± 0.004 $M_\odot$ for TOI-782, TOI-1448, TOI-2120, and TOI-2406, respectively. We adopted these values as our fiducial values for M_s, which are listed in Table 4.

Next, we updated $T_{\rm eff}$, R_s, and d by fitting a stellar-atmospheric model to the SED constructed from the photometric magnitudes. For the photometric magnitudes, we used the catalog magnitudes in the BP, G, RP bands from Gaia DR3, J, H, K_s bands from 2MASS, and W1, W2 from AllWISE (Wright et al. 2010; Mainzer et al. 2011) for all host stars except for TOI-2120. For TOI-2120, because there is a nearby background star (TIC 389900766) that was separated from TOI-2120 by ∼9″, ∼6″, and ∼4″ at the times when the data were collected by 2MASS, AllWISE, and Gaia, respectively, we did not use the W1 and W2 magnitudes from AllWISE, which could be contaminated by the flux from this nearby star. For the fitting, the tabulated BT-Settl model (Allard et al. 2011) was linearly interpolated to calculate a synthetic SED for given $T_{\rm eff}$, [Fe/H], and $\log g$. We performed a Markov Chain Monte Carlo (MCMC) analysis using `emcee` (Foreman-Mackey et al. 2013) to calculate the posterior probability distributions of $T_{\rm eff}$, R_s, and d, where we applied normal priors to $T_{\rm eff}$, R_s, and d with the mean and standard deviation estimated from IRD, the empirical relation, and Gaia DR3, respectively. The [Fe/H] and M_s values are taken from Gaussian distributions with the mean and standard deviation estimated from IRD and the empirical relation. We calculated $\log g$ from the given R_s and M_s. A single jitter term was added to all the magnitude errors in quadrature and left free in the MCMC analysis. Note that we assumed no interstellar extinction, which is negligible for all the four stars according to the 3D extinction map of Green et al. (2019).[58] As a result, we obtained the values of $T_{\rm eff}$ to be $3370\ ^{+29}_{-32}$ K, $3412\ ^{+28}_{-32}$ K, 3131 ± 30 K, and $3100\ ^{+31}_{-24}$ K, and values of R_s of 0.413 ± 0.008 $R_\odot$, 0.380 ± 0.007 $R_\odot$, 0.245 ± 0.006 $R_\odot$, and 0.204 ± 0.004 $R_\odot$ for TOI-782, TOI-1448, TOI-2120, and TOI-2406, respectively. The updated values of $T_{\rm eff}$ are consistent with those derived from the IRD spectra (Section 3.1.1) within 1σ for TOI-782, TOI-1448, and TOI-2120 and within 2σ for TOI-2406. The updated values of R_s are all within 1σ of those derived from the empirical relation. Our values of $T_{\rm eff}$, R_s, and d are listed in Table 4. The prior and posterior SED models along with the fitted SED data are shown in Figure 12.

3.1.3. Stellar Activity and Rotation

In order to investigate the magnetic activity and rotation periods of the host stars, we searched for long-term photometric variability of the host stars in the TESS light curves. We found no significant variability in any of the four stars. We also searched for periodic variability in the g- and r-band archival light curves of Zwicky Transient Facility (ZTF) DR16,[59] which are available for TOI-1448, TOI-2120, and TOI-2406, and in the g- and V-band light curves from ASAS-SN[60] for TOI-782, by performing a Lomb–Scargle periodogram analysis. As a result, there were no plausible periodic signals in any of the

[58] http://argonaut.skymaps.info
[59] https://irsa.ipac.caltech.edu/Missions/ztf.html
[60] https://asas-sn.osu.edu/

Table 4
Properties of the Four M Dwarf Hosts

Parameters	Unit	Values				
		TOI-782	TOI-1448	TOI-2120	TOI-2406	
					This work	Wells et al. (2021)
TIC		429358906	343628284	389900760	212957629	
Gaia DR3 ID		3518374197418907648	2189711770761074816	513299860904522752	2528453161326406016	
R.A.[a]		12:15:40.8810	21:5:17.7597	01:34:1.7802	00:35:13.4606	
Decl.[a]		−18:54:37.234	+57:46:15.908	+65:30:50.248	−03:22:19.668	
pmRA[a]	mas yr^{-1}	-163.739 ± 0.023	-15.617 ± 0.020	306.045 ± 0.014	226.011 ± 0.052	
pmDec[a]	mas yr^{-1}	-36.597 ± 0.020	-64.690 ± 0.019	-215.453 ± 0.019	-336.242 ± 0.035	
Parallax[a]	mas	19.153 ± 0.020	13.585 ± 0.015	31.072 ± 0.018	17.985 ± 0.041	
T (TESS)	mag	12.2875 ± 0.0073	13.1717 ± 0.0074	12.8233 ± 0.0074	14.3109 ± 0.0074	
G (Gaia)	mag	13.5428 ± 0.0004	14.3794 ± 0.0006	14.1593 ± 0.0005	15.6630 ± 0.0006	
BP (Gaia)	mag	15.0559 ± 0.0016	15.7910 ± 0.0030	15.9017 ± 0.0028	17.4339 ± 0.0060	
RP (Gaia)	mag	12.3426 ± 0.0007	13.2132 ± 0.0013	12.9023 ± 0.0009	14.3930 ± 0.0012	
J(2MASS)	mag	10.675 ± 0.021	11.599 ± 0.030	11.100 ± 0.023	12.633 ± 0.024	
H (2MASS)	mag	10.108 ± 0.024	11.033 ± 0.030	10.452 ± 0.026	12.129 ± 0.024	
K (2MASS)	mag	9.860 ± 0.024	10.765 ± 0.020	10.205 ± 0.023	11.894 ± 0.025	
W1 (WISE)	mag	9.717 ± 0.022	10.628 ± 0.022	⋯	11.706 ± 0.023	
W2 (WISE)	mag	9.559 ± 0.020	10.509 ± 0.020	⋯	11.458 ± 0.022	
Mass	$M_\odot$	0.397 ± 0.010	0.372 ± 0.009	0.211 ± 0.005	0.166 ± 0.004	0.162 ± 0.0008
Radius	$R_\odot$	0.413 ± 0.008	0.380 ± 0.007	0.245 ± 0.006	0.204 ± 0.004	0.202 ± 0.011
Effective temp.	K	3370^{+29}_{-32}	3412^{+28}_{-32}	3131 ± 30	3100^{+31}_{-24}	3100 ± 75
log *g*	cm s^{-2}	4.804 ± 0.021	4.849 ± 0.019	4.985 ± 0.024	$5.041^{+0.022}_{-0.020}$	$5.037^{+0.053}_{-0.051}$
Density	g cm^{-3}	$7.9^{+0.6}_{-0.5}$	$9.5^{+0.6}_{-0.5}$	$20.3^{+1.7}_{-1.5}$	$27.7^{+2.1}_{-1.7}$	$27.7^{+5.3}_{-4.2}$
Luminosity	$L_\odot$	$0.01984^{+0.00044}_{-0.00052}$	$0.01758^{+0.00030}_{-0.00033}$	$0.00517^{+0.00013}_{-0.00016}$	$0.00345^{+0.00008}_{-0.00009}$	0.0034 ± 0.00016
Distance	pc	52.210 ± 0.055	73.610 ± 0.079	32.183 ± 0.018	55.60 ± 0.12	55.6 ± 0.13
Rot. period	day	65.257 ± 0.063	42.28 ± 0.085	⋯	⋯	⋯
[Fe/H]	dex	0.34 ± 0.15	0.37 ± 0.14	0.39 ± 0.22	-0.26 ± 0.24	-0.38 ± 0.07
[Na/H]	dex	0.24 ± 0.14	0.31 ± 0.17	0.31 ± 0.25	-0.21 ± 0.28	⋯
[Mg/H]	dex	0.45 ± 0.19	0.26 ± 0.18	0.22 ± 0.30	-0.16 ± 0.39	⋯
[Ca/H]	dex	0.39 ± 0.15	0.18 ± 0.16	0.12 ± 0.27	-0.44 ± 0.35	⋯
[Ti/H]	dex	0.80 ± 0.30	0.66 ± 0.26	0.71 ± 0.38	-0.06 ± 0.31	⋯
[Cr/H]	dex	0.40 ± 0.16	0.35 ± 0.15	0.32 ± 0.22	-0.38 ± 0.18	⋯
[Mn/H]	dex	0.36 ± 0.23	0.38 ± 0.22	0.17 ± 0.36	-0.61 ± 0.41	⋯
[Sr/H]	dex	0.54 ± 0.22	0.55 ± 0.20	0.40 ± 0.30	-0.54 ± 0.37	⋯
Systemic RV	km s^{-1}	-7.8 ± 0.1	-23.7 ± 0.1	20.9 ± 0.1	-29.5 ± 0.1	⋯
U	km s^{-1}	-33.57 ± 0.13	$+22.78 \pm 0.05$	-54.39 ± 0.09	-2.35 ± 0.06	$+1.5 \pm 0.9$
V	km s^{-1}	-19.27 ± 0.12	-19.79 ± 0.10	-13.60 ± 0.09	-109.69 ± 0.44	-93.2 ± 2.1
W	km s^{-1}	-17.54 ± 0.09	-13.71 ± 0.04	-23.60 ± 0.04	-12.39 ± 0.20	-46.4 ± 5.2

Note.
[a] From Gaia DR3. The values are given for epoch = J2016.0.

light curves except for the *g*- and *r*-band ZTF light curves of TOI-1448, in which we found significant and coincident periodic signals with false alarm probabilities (FAPs) of less than 0.1%, as shown in Figure 1. The strongest signals in the power spectra for the *g* and *r* bands are present at periods of 42.32 ± 0.11 days and 42.22 ± 0.13 days, having variability amplitudes of 10.8 ± 1.8 mmag and 9.2 ± 1.5 mmag, respectively. Considering the significance and period coincidence of the two signals, we attribute these signals to stellar rotation. The weighted mean of the two periods is calculated to be 42.28 ± 0.085 days, which is listed in Table 4.

TOI-782 was observed by the HATSouth ground-based telescope network (Bakos et al. 2013) during two observing seasons between 2010 January 26 and 2013 July 23, with a gap in the observations between 2010 August 10 and 2012 December 18. A total of 25,247 photometric observations were obtained in the *r* band with an exposure time of 4 minutes. The observations were reduced to trend-filtered light curves following the procedures described in Bakos et al. (2013). We used the generalized Lomb–Scargle (GLS) periodogram (Zechmeister & Kürster 2009) to detect a significant periodic signal in the light curve at a period of $P = 64$ days, and with a semiamplitude of 7.28 ± 0.23 mmag, assuming a strictly periodic sinusoidal signal. The signal has a formal bootstrap-calibrated formal FAP of less than 10^{-200}, with the number of independent trials calibrated through a bootstrap procedure. This indicates a vanishingly small chance of white noise data producing a periodogram peak of this height. However, the signal also appears to vary over time. When we analyze the two seasons separately, the peak period in the GLS periodogram for the first season is at a period ~ 30 days, with a lower significance, while the second season shows a strong peak at $\sim$60 days. The semiamplitude of the $P = 64$ day signal is also lower in the first season, with a value ~ 2 mmag. Because of the apparent evolution of the signal with time, we also calculated the discrete autocorrelation function (DACF; Edelson & Krolik 1988) of the light curve, and find a clear cyclic variation with a period of $P = 65.653 \pm 0.051$ days

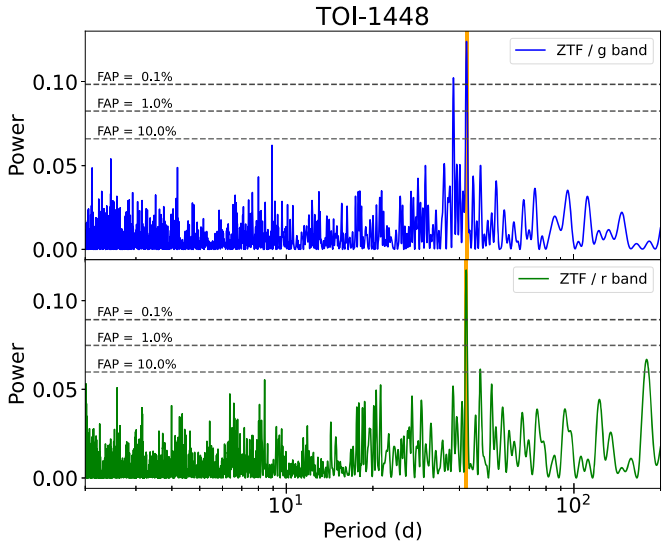

(a)

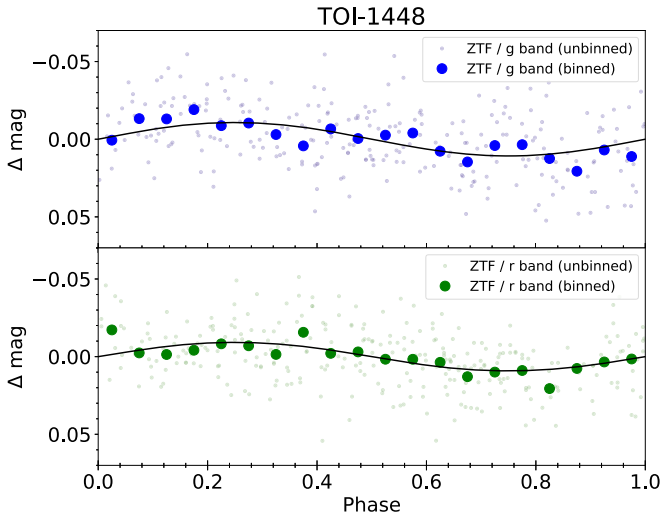

(b)

Figure 1. (a) Power spectra for the *g*- (top) and *r*-band (bottom) ZTF light curves of TOI-1448. The gray dashed lines indicate FAPs of 0.1, 1, and 10% from top to bottom. Significant, coincident signals, as shown by the orange vertical lines, can be seen at a period of 42.3 days. (b) The ZTF light curves of TOI-1448 in the *g* band (top) and the *r* band (bottom) folded with the peak periods. Light dots and dark circles are unbinned and binned data, respectively. Black curves show the best-fit sine function.

based on fitting two parabolas to the first and second prominent peaks in the DACF. Some less prominent peaks also appear at shorter time lags. The analysis discussed so far is for a partial detrending of the light curve against a set of auxiliary instrumental parameters (henceforth referred to as external parameter decorrelation (EPD)), which yields a point-to-point rms of 25 mmag. When we apply the more aggressive trend-filtering algorithm (TFA; Kovács et al. 2005) to the HATSouth light curve, which reduces the rms to 20 mmag, the signal remains at a high level of significance, but the amplitude of this long-period variation is reduced to 4.18 ± 0.22 mmag. The DACF of the TFA light curve appears to show a cleaner cyclic variation, with the lag between the first and second peaks indicating a period of $P = 65.257 \pm 0.063$ days. This suggests that the additional less pronounced, shorter-lag peaks present in the EPD DACF are likely due to instrumental artifacts. The periodogram, DACF, and light curve are shown in Figure 2.

3.2. Stellar Age

TOI-782 and TOI-1448 have a slow rotation with $P \sim 65.7$ days and 42.3 days, respectively. Neither TOI-782 nor TOI-2120 show any activity variations due to stellar spots. The low-velocity stars, TOI-782, TOI-1448, and TOI-2120, are probably thin disk stars (see Table 4), whereas the total velocity of the metal-poor TOI-2406, $v_{\rm tot} = \sqrt{U^2 + V^2 + W^2} \sim 110$ km s^{-1}, suggests that it is a member of the thick disk (see also Wells et al. 2021). In fact, the thick disk to thin disk probability ratios of TOI-782, TOI-1448, TOI-2120, and TOI-2406 are estimated to be 0.0125, 0.0144, 0.0213, and 38.9, respectively, from their Galactic kinematics (Bensby et al. 2014), respectively. Also, the BANYAN Σ analysis (Gagné et al. 2018) confirm that these four M dwarfs are not bona fide members of the young association within ∼100 pc.

3.3. Validation of the Planetary Candidates

In the following paragraphs, we qualitatively eliminate the classes of false positive scenarios that can mimic the transit signal including an EB with a grazing transit geometry, a hierarchical eclipsing binary (HEB), and a diluted eclipse of a background (or foreground) eclipsing binary (BEB) along the line of sight of the target. Although the planetary nature of TOI-2406b has already been validated by Wells et al. (2021), we will still validate all four planetary candidates for completeness.

First, the renormalised unit weight error (RUWE) from Gaia DR3[61] is 1.25, 1.08, 1.15, and 1.06 for TOI-782, TOI-1448, TOI-2120, and TOI-2406, respectively, which are all low enough to be consistent with a single star being the source of the astrometric motion (Belokurov et al. 2020). We also rule out the EB scenario based on the mass constraint derived in Section 3.4.3. Moreover, we do not detect any wavelength dependence of the transit depth from our chromatic transit analysis (Section 3.4.2), which is consistent with the absence of contamination from a star of a spectral type (color) different from the host star. In the absence of dilution, the measured planetary radii become significantly smaller than the lower limit of 0.8 $R_{\rm Jup}$ expected for brown dwarfs (Burrows et al. 2011). Grazing transit geometries can be eliminated, as the impact parameter is constrained to $b < 0.6$ at the 99% level based on our transit and contamination analyses. The apparent boxy shapes of the transit light curves are in stark contrast with the V-shaped transit expected for grazing orbits. Hence, the grazing EB scenario is ruled out.

Second, we constrain the classes of HEBs that reproduce the observed transit depth and shape using our multiband observations. We aim to compute the eclipse depths for a range of plausible HEBs in the bluest and reddest bandpasses where they are expected to vary significantly. We adopt the method presented in Mori et al. (2022), which is based on Bouma et al. (2020), to perform the calculation over a grid of eclipsing companions.[62] Comparing the simulated eclipse depth with the observed one (Section 3.4.2) in each band, we find that no plausible HEB configuration explored in our

[61] https://gaia.ari.uni-heidelberg.de/singlesource.html

[62] We assumed cases where the impact parameter is allowed to vary from zero to one.

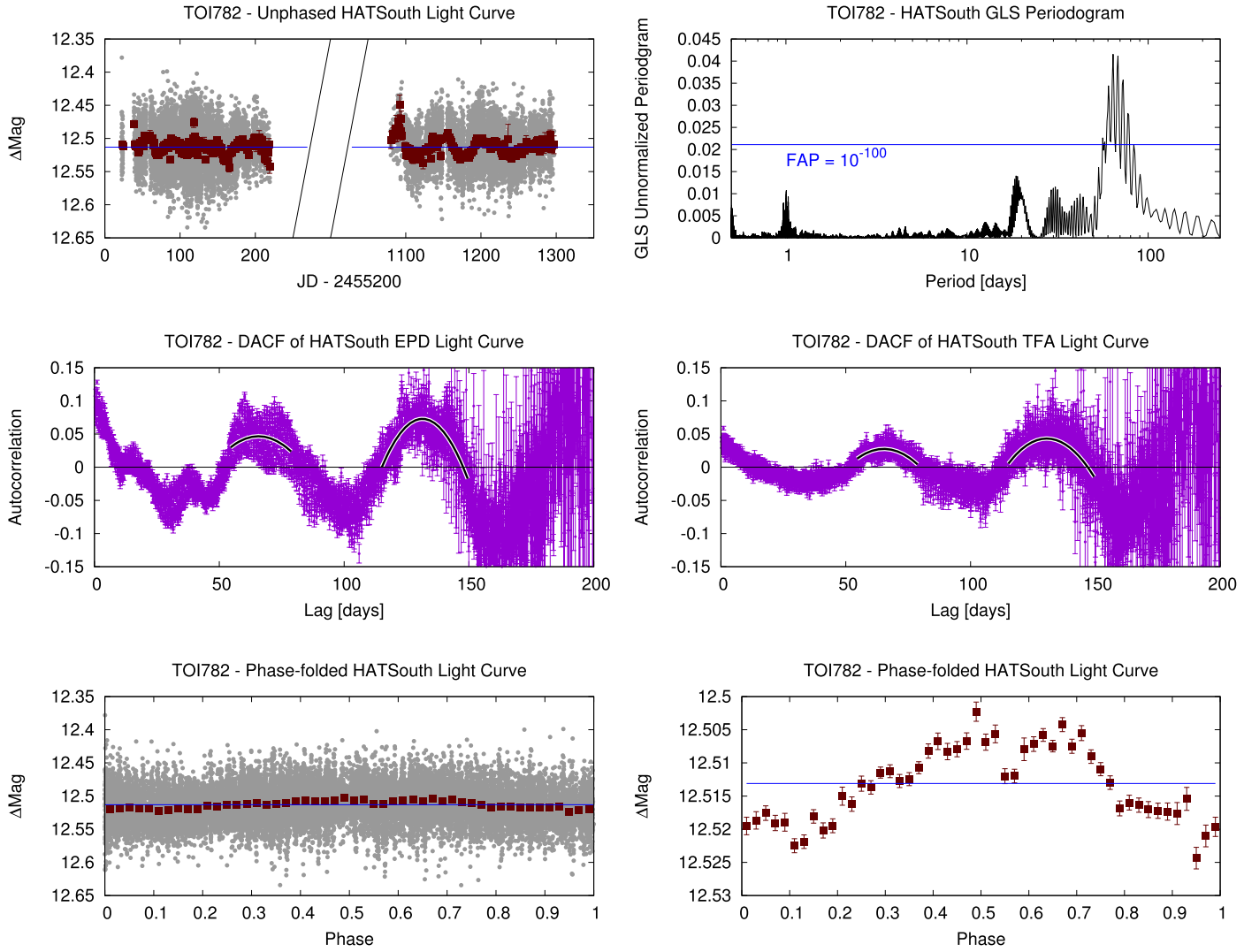

Figure 2. Top left: the HATSouth light curve of TOI-782 plotted against time. The gray points show the unbinned data, while the red squares show the data binned by 1 day. For clarity, we cut out a gap in the data as shown. The light curve shown in this figure has had an EPD detrending applied to it, but not the more aggressive TFA detrending that is typically also applied to HATSouth light curves. Top right: the GLS unnormalized periodogram of the HATSouth light curve of TOI-782 shows a strong peak at a period of $P = 64$ days. Middle left: the DACF of the HATSouth EPD light curve. The first and second prominent peaks are fitted with parabolas to determine the period. Middle right: same as on the left, but here we show the DACF of the HATsouth TFA light curve. Some shorter-lag variations in the EPD DACF are not present, suggesting that they are likely due to instrumental systematics. Bottom left: the HATSouth EPD light curve phase folded at the detected period. The gray-scale points show the unbinned data, while the red squares show the phase-binned data with a bin size of 0.02. Bottom right: same as on the left, but here we show only the phase-binned data and zoom in to see the detected photometric variation more clearly.

simulation can reproduce the observed transit depths in the multiple bands simultaneously as well as the transit shape. To check the possibility of stellar companions spectroscopically, we visually searched for secondary peaks in the stellar line profiles. For all the four targets, the mean line profile, a cross-correlation function of the IRD spectra against a template spectrum, exhibited no sign of a stellar companion with a contrast higher than ∼0.1 in the near-infrared wavelengths. Hence, the HEB scenario is ruled out.

Third, the probability of being a BEB is low a priori because our targets are far from the Galactic plane, except for TOI-1448 and TOI-2120,[63] and we argue below that the BEB scenario for TOI-1448 and 2120 is very unlikely. First, there is a background star (TIC 389900766; $\Delta G = 5.1$) near TOI-2120 with a separation of 2.″2–2.″5 at the times of the ground-based transit observations, which contaminates the photometric apertures for these observations (3″ or larger in radius). However, we did not detect any significant chromatic difference in the transit depth in the analysis of the ground-based transit light curves (Section 3.4.2), which cannot be explained by the BEB scenario given the chromatic flux ratios of the background star to TOI-2120 of 1.3%, 1.6%, 0.78%, and 0.79% for the g, r, i, and z_s bands, respectively, measured from the Pan-STARRS1 catalog (Chambers et al. 2016). Next, our high-resolution speckle and AO imaging ruled out any other nearby star and blended sources down to 0.″5 at a Δmag of 7.7 (2166 nm), 7.0 (2166 nm), 5.6 (832 nm), and 5.2 (832 nm) for TOI-782, TOI-1448, TOI-2120, and TOI-2406, respectively. We statistically estimate the probability of a chance-aligned star, using the population synthesis code `TRILEGAL`[64] (Girardi et al. 2005), which simulates the Galactic stellar population

[63] TOI-1448 and 2120 have Galactic latitudes of $b = +7.^{\circ}1234$ and $b = +3.^{\circ}007295$, respectively.

[64] http://stev.oapd.inaf.it/cgi-bin/trilegal

Table 5
Posterior Values of the Parameters Used in the Joint Fitting

Parameters	Unit	Values			
		TOI-782 b	TOI-1448 b	TOI-2120 b	TOI-2406 b
P	days	$8.0240015^{+0.0000077}_{-0.0000072}$	8.112245 ± 0.000018	5.7998164 ± 0.0000035	3.0766891 ± 0.0000024
$T_{c,0}$	BTJD[a]	$1577.04189^{+0.00085}_{-0.00093}$	1713.3375 ± 0.0015	1795.82368 ± 0.00041	$2115.97600^{+0.00031}_{-0.00029}$
b		$0.46^{+0.12}_{-0.25}$	$0.21^{+0.16}_{-0.14}$	$0.55^{+0.07}_{-0.10}$	$0.09^{+0.09}_{-0.06}$
k		0.0606 ± 0.0015	0.0663 ± 0.0011	0.0796 ± 0.0014	0.1287 ± 0.0013
ρ_s	g cm^{-3}	7.99 ± 0.54	9.51 ± 0.55	$20.6^{+1.7}_{-1.5}$	27.4 ± 1.9
$\sqrt{e}\sin\omega$		$0.31^{+0.14}_{-0.19}$	$-0.03^{+0.13}_{-0.15}$	$0.48^{+0.08}_{-0.10}$	$-0.31^{+0.05}_{-0.04}$
$\sqrt{e}\cos\omega$		0.05 ± 0.33	$-0.01^{+0.30}_{-0.27}$	$0.07^{+0.33}_{-0.35}$	$0.10^{+0.30}_{-0.36}$
K	m s^{-1}	$5.7^{+3.3}_{-3.0}$ (<11.6)	<12.5	<7.3	<23.7
γ	m s^{-1} d^{-1}	...	0.041 ± 0.019	-0.045 ± 0.007	...
$\sigma_{\rm rv,jitter}$	m s^{-1}	$9.0^{+2.1}_{-1.7}$	$13.0^{+4.0}_{-2.9}$	3.5 ± 2.0	$4.7^{+5.9}_{-3.3}$

Note. The reported values, uncertainties, and upper limits represent the median, 1σ lower and upper boundaries, and 2σ upper boundaries of the posterior probability distributions, respectively.
[a] Barycentric TESS Julian Date, which corresponds to Barycentric Julian Date (BJD) - 2457000.

along any line of sight. Given the positions of our targets, we found probabilities of $P_{\rm BEB} < 10^{-6}$ to find a star brighter than $T_{\rm mag} \simeq 16$,[65] within $0\farcs5$. Assuming that all such stars are binaries and preferentially oriented edge on to produce eclipses with the period and depth consistent with the TESS detection, this can represent a conservative upper limit to the BEB scenario.

Finally, we quantify the false positive probability (FPP) of our targets using the Python package `TRICERATOPS` (Giacalone et al. 2021). We used the ephemerides and depths reported in Table 5, the contrast curves from the high-resolution images with the highest contrast achieved, and the MuSCAT3 i-band follow-up light curves as inputs to `TRICERATOPS`. Although we were able to rule out the classes of EB, BEB, and HEB, we ran `TRICERATOPS` considering all of these scenarios for completeness. We obtained formal FPPs of the order of 10^{-5}, 10^{-4}, 10^{-7}, and 10^{-5} for TOI-782 b, TOI-1448 b, TOI-2120 b, and TOI-2406 b, respectively. These values are well below the threshold of FPP $< 1.5\%$ prescribed by Giacalone et al. (2021) which statistically validates them as bona fide planets.

3.4. Properties of the Planets

To derive the physical properties of the planets, we analyzed the TESS light curves, ground-based transit light curves, and RV data of each planetary system in the following steps. First, we modeled the TESS light curves with a transit + Gaussian process (GP) model to determine the hyperparameters of the GP model. Next, we modeled the ground-based transit light curves with a transit + GP model using the posteriors of the transit parameters obtained from the above analysis as priors and then determined the hyperparameters of the GP model for the ground-based data. Finally, we jointly modeled all the light curves and RV data with transit and RV models along with the predetermined hyperparameters of the GP models to derive the final values and uncertainties of the planetary parameters. We describe each step in more detail in the following subsections.

[65] $T_{\rm mag}$ denotes the TESS magnitude. The maximum Δmagnitude was computed using $dT = -2.5\log_{10}$(depth), which translates to the magnitude that can produce a 100% eclipse.

3.4.1. TESS Light Curves

For the transit model, we adopted the Mandel & Agol (2002) model implemented by `PyTransit` (Parviainen 2015) with the following parameters: scaled semimajor axis $a_R (= a/R_s$, where a is the semimajor axis), impact parameter b, planet-to-star radius ratio $k (= R_p/R_s$, where R_p is the planetary radius), eccentricity e, the argument of periastron ω, orbital period P, individual transit times $T_{c,i}$, and two coefficients u_1 and u_2 of a quadratic limb-darkening law. Note that the model is super-sampled, i.e., averaged over the exposure time. At this stage, we set both e and ω to zero and P to the value provided by the TOI catalog. For u_1 and u_2, we applied Gaussian priors with the values and uncertainties of the stellar parameters given by `LDTk` (Parviainen & Aigrain 2015). Note that we increased the uncertainties of u_1 and u_2 given by `LDTk` by a factor of 3 to account for the possible systematics in the stellar models. We assumed uniform priors for the other parameters.

Simultaneously with the transit model, we also modeled the time-correlated noise in the light curves using a GP model implemented in `celerite` (Foreman-Mackey et al. 2017) with a stochastically driven, damped simple harmonic oscillator (SHO) kernel function, where the model parameters are the frequency of the undamped oscillation ω_0, the scale factor to the amplitude of the kernel function S_0, and the quality factor $\mathcal{Q}$. We set $\mathcal{Q}$ to unity in all sectors to avoid overfitting, while leaving ω_0 and S_0 free for each sector to account for the different noise properties from sector to sector. We also fit a white jitter term in the flux for each sector. We ran an MCMC analysis for each target using `emcee` to estimate the posterior distributions of the parameters.

3.4.2. Ground-based Light Curves

We simultaneously modeled the ground-based, multiband transit light curves of each target with a transit + GP model. We used the same transit model as described in Section 3.4.1, but left k free for each band in order to search for chromaticity in k, which can be a sign of flux contamination in the photometric aperture. The limb-darkening parameters u_1 and u_2 were fitted with Gaussian priors for each band in the same way as for the TESS light curves. Note that all the measured fluxes of TOI-2120 are contaminated by a nearby faint background star (TIC 389900766), as mentioned in Section 3.3. We,

therefore, corrected the contamination to TOI-2120 b by replacing the transit model $\mathcal{F}_{\rm tr}$ with $(\mathcal{F}_{\rm tr} + f_{\rm cont})/(1 + f_{\rm cont})$, where $f_{\rm cont}$ is the flux ratio of the target to the contaminating source (1.3%, 1.6%, 0.78%, and 0.79% for the g, r, i, and z_s bands, respectively, assuming that all the fluxes were contaminated in the photometric apertures). The time-correlated noise in the ground-based light curves was computed by a GP model as a function of time in the `celerite` package whose covariance function is an approximate Matérn $3/2$ kernel with signal standard deviation σ and length scale ρ. The kernel function has the same ρ in all light curves of each transit event but different σ. Note that this kernel is a specific version of the SHO kernel (Section 3.4.1) with no oscillation term. We applied this simplified form to the ground-based light curves considering that their observational durations are shorter than the stellar variability timescale. The MuSCAT2 data exhibit nonnegligible systematics arising from telescope drifts. Therefore, for the time-correlated noise model of the MuSCAT2 data, we multiplied the GP model by a linear function of Δx and Δy, where Δx and Δy denote stellar displacements in the detector in the x- and y-directions, respectively. We performed an MCMC analysis for each target using `emcee` with uniform priors for all parameters except for u_1 and u_2.

3.4.3. Joint Analysis of the Radial Velocities and Light Curves

From a preliminary analysis of the RV data, we did not detect significant ($>3\sigma$) planetary signals in any of the systems. Nonetheless, the RV data are still useful for placing upper bounds on the planetary masses and orbital eccentricities. Because both the RV and transit light-curve models depend on eccentricity, the best constraint on the mass and eccentricity can be obtained by a joint analysis of the RV and transit light-curve data. We therefore simultaneously modeled the RV data and all the available transit light curves (from both TESS and the ground) of each system. The parameters of the RV model include RV amplitude K, orbital inclination i, eccentricity parameters e and ω (fitted as $\sqrt{e}\sin\omega$ and $\sqrt{e}\cos\omega$), orbital period P, time of periastron passage t_0, RV offset v_0, and RV jitter $\sigma_{v,\rm jit}$. We additionally included a parameter for a linear slope in the RV, γ, for the data of TOI-1448 b and TOI-2120 b, for which a preliminary fit of the RV data only indicated that a model with a linear slope was preferred over a model without a slope, determined by the corresponding values of the Bayesian information criterion, ΔBIC, of 3.8 and 21.8, respectively. The parameters for the transit model are the same as in Section 3.4.2, but this time the assumption of a circular orbit was removed. In addition, we assumed a constant orbital period, which introduces a reference transit time $T_{\rm c,0}$ for each system, because we did not detect significant variations in the individual transit timings ($T_{{\rm c},i}$) measured in the TESS and ground-based light curves from a constant period in any system. We also adopted a constant radius ratio k across the bands for each system because we did not detect any significant chromaticity in k in the analyses of Sections 3.4.1 and 3.4.2. The hyperparameters of the GP for the TESS and ground-based light curves were set to the best-fit values derived in Sections 3.4.1 and 3.4.2, respectively, to suppress the number of free parameters. Note that the correlations between the hyperparameters and other physical parameters are small enough that fixing the hyperparameters at the best-fit values does not have much effect on the posterior distributions of the hyperparameters.

With the above parameterization, we performed an MCMC analysis using `emcee`. Note that in this analysis i and t_0 are not fitted but i is converted from b, a_R, e, and ω by the equation of $b = a_R \cos i (1 - e^2)/(1 + e\sin\omega)$ and t_0 is converted from $T_{\rm c,0}$, P, and Kepler's equation. In addition, we use log stellar density $\log\rho_s$ as the fitting parameter instead of a_R, which is converted from ρ_s and P by the equation $a_R = (\rho_s G P^2/3\pi)^{1/3}$ (assuming $k^3 \ll 1$), where G is the gravitational constant.

For the priors, we applied a two-sided Gaussian distribution for ρ_s using the values derived in Section 3.1.2. We also applied the joint probability distribution for e and ω of Kipping (2014, Equation (23) in that paper), which is a conditional probability given that the planet has a transit geometry adopting a beta function as the underlying prior for e. For the two coefficients of the beta function, we adopted $\alpha = 1.58$ and $\beta = 4.4$ from Van Eylen et al. (2019), which were derived from a sample of Kepler single-transiting systems. Uniform priors were applied to all the other parameters.

The derived posterior values (median and 1σ boundaries or 2σ upper limits) are listed in Table 5. The transit light curves detrended and phase folded by the best-fit parameters, and the time series and phase-folded RV data along with the posterior RV models, for TOI-782 b, TOI-1448 b, TOI-2120 b, and TOI-2406 b are shown in Figures 3, 4, 5, and 6, respectively.

3.4.4. Results

Combining the results of the joint analysis in Section 3.4.3 with the stellar properties derived in Section 3.1.2, we derive the physical properties of the planets as listed in Table 5. We find that TOI-782 b, TOI-1448 b, TOI-2120 b, and TOI-2406 b have radii of $2.734 \pm 0.085\ R_\oplus$, $2.749^{+0.067}_{-0.063}\ R_\oplus$, $2.122 \pm 0.065\ R_\oplus$, and $2.860^{+0.063}_{-0.069}\ R_\oplus$, respectively, all of which are within the sub-Neptune regime. Our value for TOI-2406 b is consistent with that measured by Wells et al. (2021) within the uncertainties but is more precise thanks to the additional TESS data taken after their work and our high-precision multiband transit light curves taken with MuSCAT3.

Two-dimensional posterior distributions between M_p, e, and ω obtained from the joint analysis are shown in blue in Figure 7. Although we are unable to measure the masses of any of the planets with a high enough significance, we place 2σ upper limits on the masses of 19.1, 19.5, 6.8, and 15.6 $M_\oplus$ for TOI-782 b, TOI-1448 b, TOI-2120 b, and TOI-2406 b, respectively (see Figure 8). We find tentative linear trends in the RV data of TOI-1448 and TOI-2120 with $\gamma = 0.041 \pm 0.019$ and -0.044 ± 0.007 m s^{-1} day^{-1}, respectively, which could be due to an additional outer planet or companion, or some unrecognized systematics. Further RV observations are needed to determine the definitive masses of these planets and to confirm or refute the presence of outer planets/companions to TOI-1448 b and TOI-2120 b.

While we cannot unambiguously determine the eccentricity due to the lack of significant planetary signals in the RV data, our joint analyses of the RV data and transit light curves with stellar density priors show that three of the four planets, TOI-782 b, TOI-2120 b, and TOI-2406 b, have nonzero eccentricities with significances of $\sim$2–4σ ($0.19^{+0.09}_{-0.11}$, 0.32 ± 0.08, and $0.17^{+0.11}_{-0.05}$, respectively). These eccentricities are mostly constrained by the transit light curves with the stellar density priors. To illustrate this, in Figure 7 we overplot the posterior distributions of M_p, e, and ω obtained from analyses of the RV data alone (where $T_{c,0}$, P, and i are fixed to the values measured

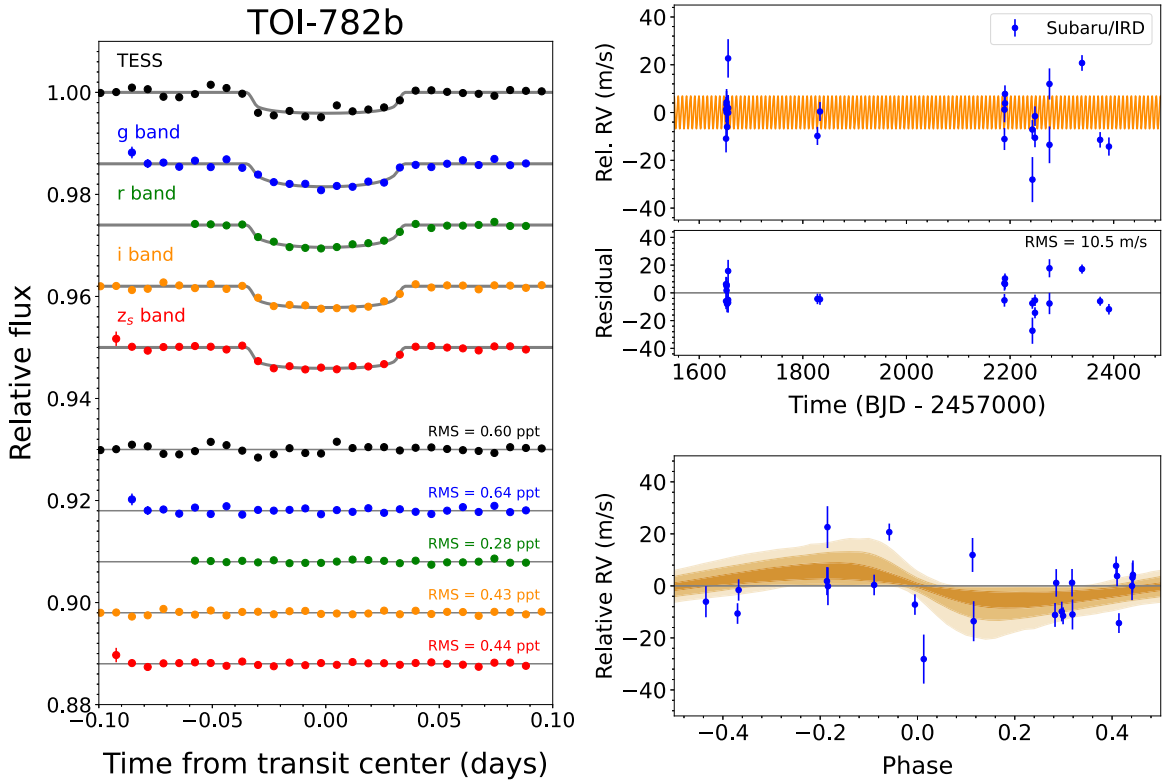

(a) (b)

Figure 3. (a) Detrended and phase-folded light curves of TOI-782 b (upper five curves) and their residuals from the best joint-fitting model (lower five curves). The black, blue, green, orange, and red points (from top to bottom in each of the five data sets) indicate 5 minutes binned data from the TESS, g, r, i, and z_s bands, respectively. Gray lines indicate the best-fit models. The plots are vertically shifted for display. (b) Top: time series of RV data from Subaru/IRD (blue) along with the 1σ, 2σ, and 3σ credible regions calculated from the posteriors of the joint-fitting analysis (from thick to thin orange). Error bars represent the estimated 1σ uncertainties without a jitter term. Middle: residuals of the RV data from the best joint-fitting model. Bottom: same as the top panel, but phase folded with the orbital period of TOI-782 b. Areas from dark to light orange indicate 1, 2, and 3σ credible regions, respectively.

in the transit light curves) in yellow, and the posterior distributions of e and ω from analyses of the transit light-curve data alone (both TESS and ground-based ones) in red. We note that our conclusion that three of the four planets are likely to have a nonzero eccentricity does not depend on the prior on the eccentricity; we also detect nonzero eccentricities for TOI-782 b, TOI-2120 b, and TOI-2406 b at similar significances even with a uniform prior on e. We further note that a nonzero eccentricity of TOI-2406 b was originally found by Wells et al. (2021, with a uniform prior on e, and we confirmed it with almost independent transit data (except for TESS Sectors 3 and 30) and new constraints from the RVs.

4. Discussion

In this study, we discovered and followed up four single sub-Neptunes transiting nearby (<100 pc) M dwarfs. Although these four planets are not outliers in the radius–period diagram among known close-in sub-Neptunes around M dwarfs (see Figure 9), we found that at least three of them are likely to have eccentric orbits with $e \sim 0.2$–0.3, which are slightly larger than the majority of known close-in sub-Neptunes with orbital periods of $\lesssim$10 days (see Figure 10). One possible explanation for the nonzero eccentricities of these planets is that there is an unseen (long-period) planet (e.g., Limbach & Turner 2015) or a substellar companion (e.g., Ngo et al. 2016) in each system. Once the disk gas has dissipated, the eccentricity of a planet can be excited by other planets and (sub-)stellar companions through gravitational perturbations, such as planet–planet scattering (e.g., Weidenschilling & Marzari 1996) and the von Zeipel–Lidov–Kozai mechanism (e.g., Fabrycky & Tremaine 2007). In fact, TOI-1448 b and TOI-2120 b may have an unseen siblings as suggested by the linear trend in the RV data (see Figure 5).

Another dynamical process that influences the eccentricity of a close-in planet is tidal interaction between the planet and its host star. As an eccentric planet approaches to its host star, tidal forces circularize its orbit. Nonzero eccentricities of the close-in sub-Neptunes may suggest that tidal circularization of the planet's orbit is not achieved because the host star is too young or because inefficient tidal dissipation occurs in the planetary interior. The estimated ages of the four M dwarfs are all older than 1 Gyr (see Section 3.2). Therefore, all four sub-Neptunes should experience tidal forces from their host stars over 1 Gyr. The nonzero eccentricities of at least three of the sub-Neptunes are suggestive of less efficient tidal dissipation in their interiors.

We consider the tidal evolution of the three short-period sub-Neptunes in eccentric orbits around relatively old M dwarfs (see Table 6). A tidal interaction between a short-period planet and an M dwarf circularizes the orbit of the planet over gigayears. The eccentricity damping of a planet in equilibrium tide (e.g., Murray & Dermott 1999) is written as

$$\tau_e = -\frac{e}{\dot{e}} = \frac{4}{63}\frac{M_{\rm p}}{M_\star}\left(\frac{a}{R_{\rm p}}\right)^5 \frac{\tilde{\mu}_{\rm p} Q_{\rm p}}{\Omega}, \quad (1)$$

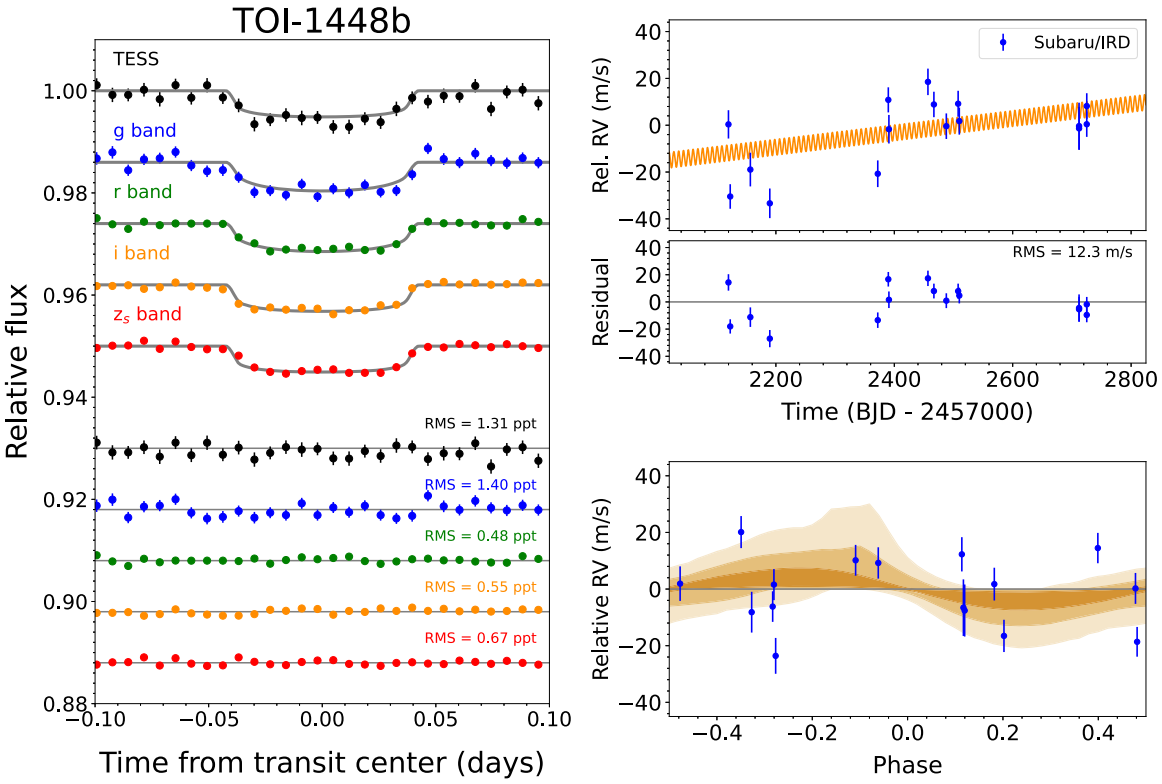

(a) (b)

Figure 4. Same as Figure 3 but for TOI-1448 b.

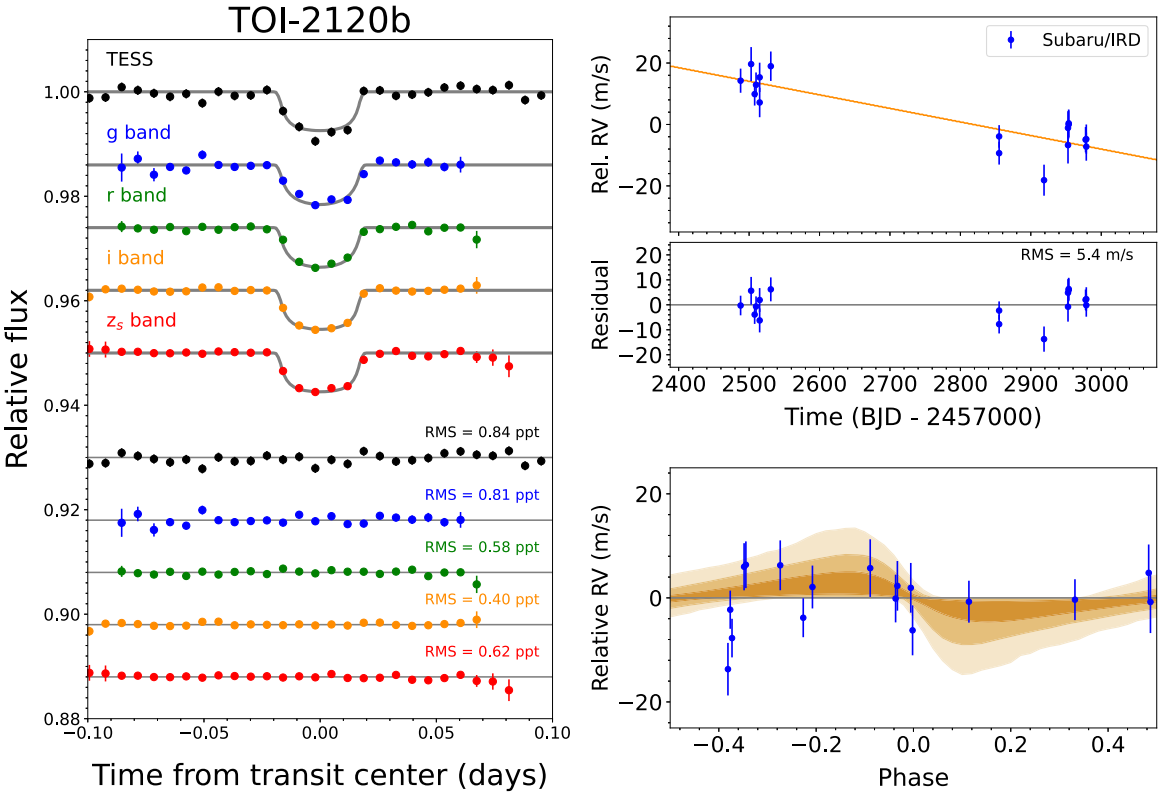

(a) (b)

Figure 5. Same as Figure 3 but for TOI-2120 b. A linear trend in the RV data was injected in the joint analysis of TOI-2120.

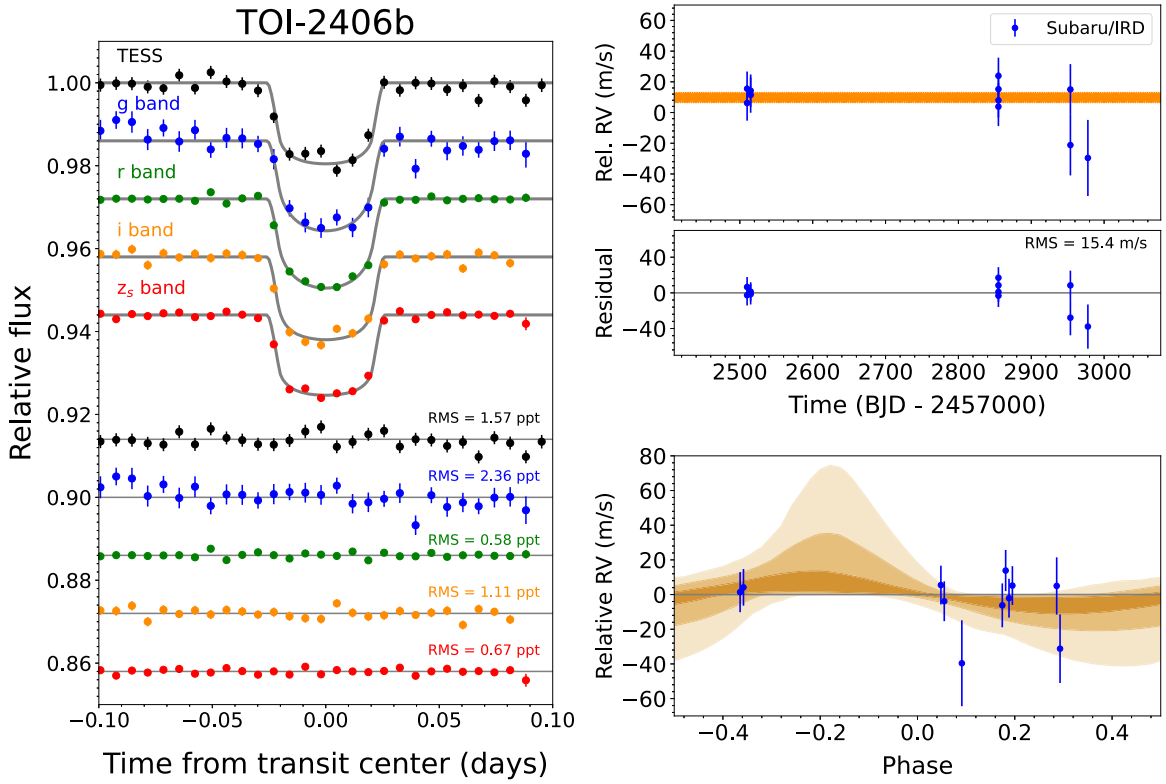

(a) (b)

Figure 6. Same as Figure 3 but for TOI-2406 b.

where e is the eccentricity of the planet, M_p is the planetary mass, R_p is the planetary radius, a is the semimajor axis, $\tilde{\mu}_p$ is the effective bulk modulus, Q_p is the tidal dissipation factor of the planet, $M_\star$ is the mass of the host star, and Ω is the Keplerian angular velocity. Figure 11 shows the eccentricity damping timescales of the three sub-Neptunes. We adopt the upper limit masses of TOI-782 b, TOI-2120 b, and 2406 b. A nonzero eccentricity for each planet can persist over gigayears if the Q value is $\gtrsim 10^3$ for TOI-782 b and TOI-2120 b, and $\gtrsim 10^5$ for TOI-2406 b, assuming that $\tilde{\mu}_p \sim 1$ and Q_p is constant for 1 Gyr. A typical Q value for a terrestrial planet and a gas giant is 10–100 and 10^5–10^6, respectively. We consider here that massive rocky planets may have a Q value greater than 10–100. Massive rocky planets have magma oceans for a long period of time due to high pressures and temperatures in their interiors. Tidal damping in rocky super-Earths can be less efficient due to the size effect (Efroimsky 2012). Tidal dissipation in massive rocky planets may be weaker than that in terrestrial planets. On the other hand, the observed eccentricity of super-Earths suggests that their typical Q value is ∼10–100 (Hansen & Murray 2015), for example, $Q_p \sim 100$ for CoRoT-7 b (Clausen & Tilgner 2015). The interiors of these three eccentric sub-Neptunes with large Q values are different from those of close-in super-Earths like CoRoT-7 b. In fact, the mass–radius relationship of these four sub-Neptunes supports that they are not composed of pure rock (see Figure 8). The four validated planets, as well as K2-18 b (e.g., Madhusudhan et al. 2023) and TOI-270 d (Benneke et al. 2024; Holmberg & Madhusudhan 2024), may be interesting targets for atmospheric characterization of sub-Neptunes. Recently, Luque & Pallé (2022) showed that planets with radii larger than 1.5 $R_\oplus$ around M dwarfs have either water-rich interiors or significant atmospheres. These interior models are consistent with planet formation models in the course of orbital migration (e.g., Venturini et al. 2020; Burn et al. 2021), followed by the photoevaporation scenario of planets with different bulk compositions (e.g., see Figure 7 in Owen & Wu 2017).

Other known eccentric, sub-Neptunes close to M dwarfs, K2-25 b with $R_p = 3.44 \pm 0.12$ $R_\oplus$, $M_p = 24.7^{+5.7}_{-5.2}$ $M_\oplus$, and $e = 0.43 \pm 0.05$ in the Hyades star cluster (600–800 Myr; Mann et al. 2016; Stefansson et al. 2020) and TOI-269 b with $R_p = 2.77 \pm 0.12$ $R_\oplus$, $M_p = 8.8 \pm 1.4$ $M_\oplus$, and $e = 0.425^{+0.082}_{-0.086}$ (Cointepas et al. 2021) around an old M dwarf with an age of a few gigayears, have drawn attention to the dynamical histories of close-in planets. K2-25 b and TOI-269 b can remain in an elliptical orbit until the present day if $Q_p \gtrsim 10^4$–10^5 (see Figure 11). These Q values larger than those of terrestrial planets are consistent with low bulk densities of both planets, indicating the presence of volatile material in their interiors.

5. Summary

We report the discovery and follow-up of four sub-Neptunes with radii of 2–3 $R_\oplus$ and $P \lesssim 8$ days orbiting M dwarfs (TOI-782, TOI-1448, TOI-2120, and TOI-2406), three of which were newly validated by ground-based follow-up observations and statistical analyses. Our RV follow-up observations with Subaru/IRD suggest that all of the four planets are less massive than 20 $M_\oplus$ at 2σ significance. The orbits of at least three

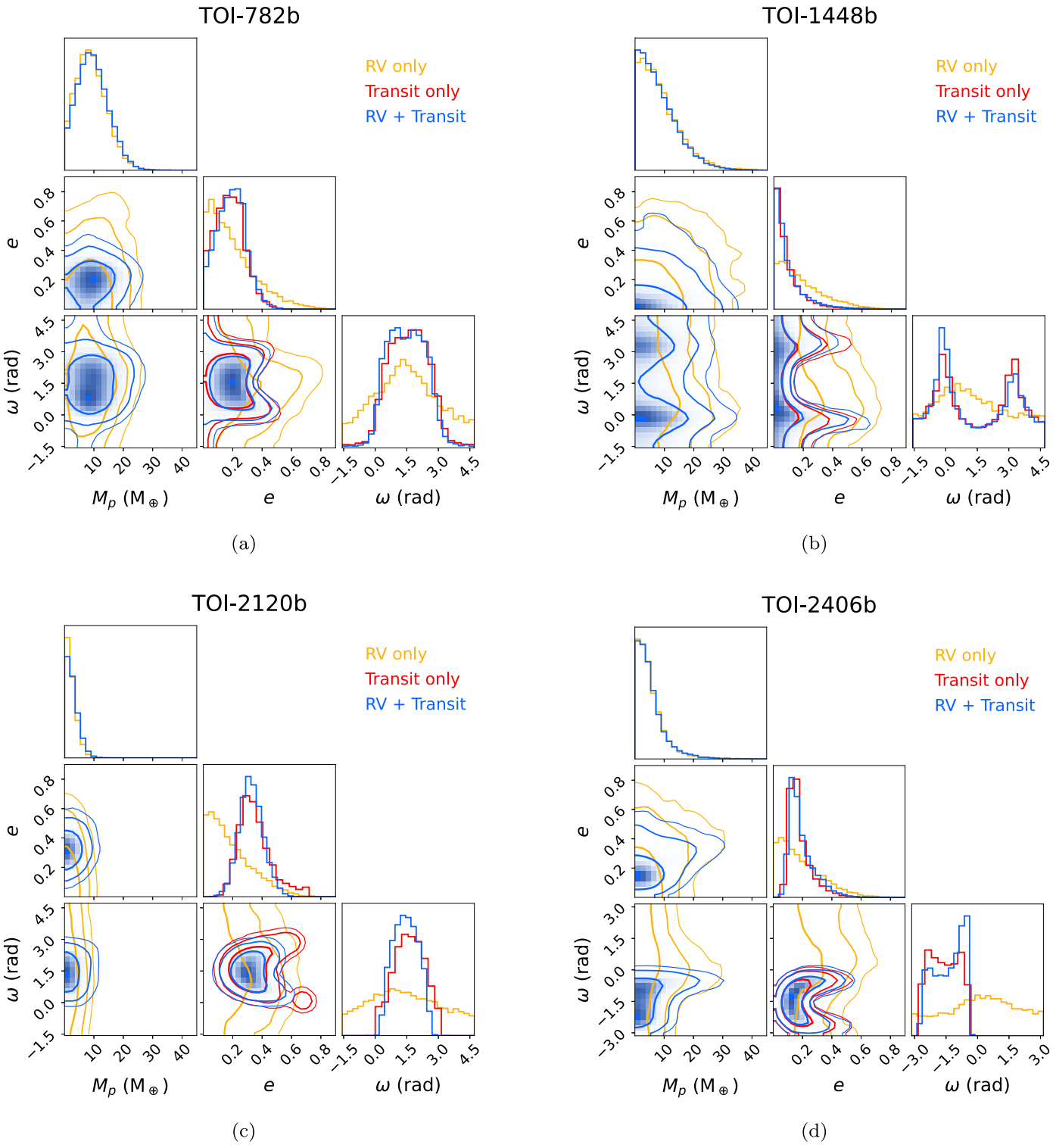

Figure 7. (a) Corner plots for the posterior samples of M_p, e, and ω for TOI-782 b. Yellow, red, and blue contours indicate the posteriors from the RV-only fit, the transit-only fit, and the RV + transit joint fit, respectively. Contours with thick to thin solid lines indicate 68%, 95%, and 99% confidence regions, respectively. The density of the posterior samples from the joint analysis is indicated by the color map. (b), (c), (d) Same as (a) but for TOI-1448 b, TOI-2120 b, and TOI-2406 b, respectively.

short-period sub-Neptunes orbiting relatively old M dwarfs with ages $\gtrsim$1 Gyr are not yet tidally circularized. The data suggest that these planets have eccentricities of $e \sim 0.2$–0.3, which would require inefficient tidal dissipation in their interiors. The slow damping of the eccentricities due to tidal interactions requires a large Q value of 10^3–10^5 for these three sub-Neptunes. The mass–radius relationship of all four sub-Neptunes suggests that they are unlikely to be pure rocky planets, that is, they have a significant atmosphere and/or an icy mantle on the core. The validated eccentric sub-Neptunes give us an unprecedented opportunity to infer the elusive interiors and formation histories of sub-Neptunes close to a central star.

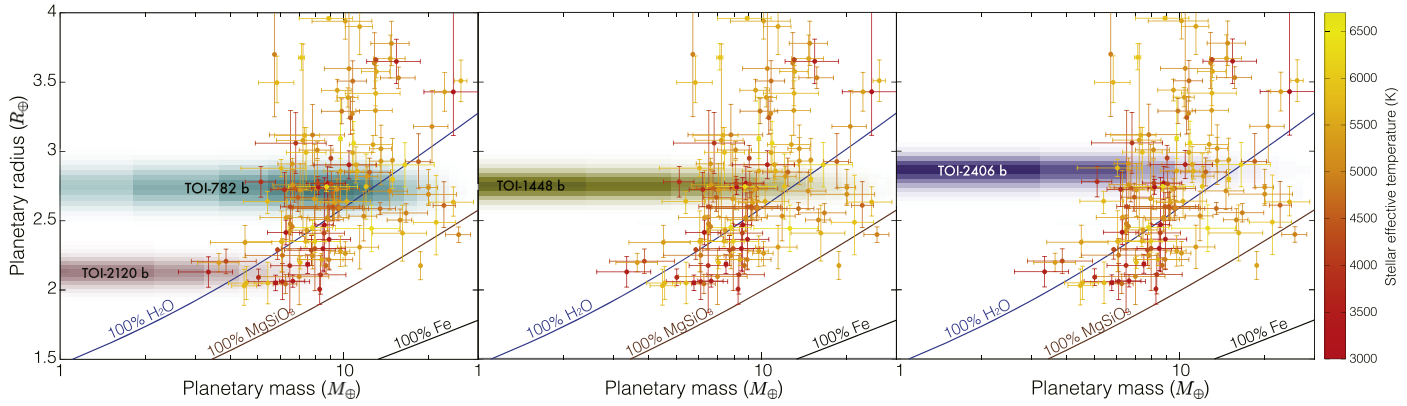

Figure 8. Mass–radius relationship of planets with measured radii of 2–4 $R_\oplus$ and orbital periods of $\lesssim$50 days around Sun-like stars and M dwarfs (data from http://www.exoplanet.eu). The curves show the interior models calculated for planets composed of pure H_2O, $MgSiO_3$, and Fe. We adopted the third-order Birch–Murnagham equation of state (EOS) for $MgSiO_3$ perovskite (Karki et al. 2000; Seager et al. 2007), the Vinet EOS for ϵ–Fe (Anderson et al. 2001), the Thomas–Fermi–Dirac EOS (Salpeter & Zapolsky 1967) at high pressure (Seager et al. 2007; Zeng & Sasselov 2013), and the AQUA EOS for H_2O (Haldemann et al. 2020). We also plotted the contours of mass ranges derived from joint analyses of the four sub-Neptunes validated in this study.

Table 6
Properties of the Four Sub-Neptunes around M Dwarfs

Parameters	Unit	Values				
		TOI-782 b	TOI-1448 b	TOI-2120 b	TOI-2406 b	
					This work	Wells et al. (2021)
Radius	$R_\oplus$	2.734 ± 0.085	$2.749^{+0.067}_{-0.063}$	2.122 ± 0.065	$2.860^{+0.063}_{-0.069}$	$2.94^{+0.17}_{-0.16}$
Mass	$M_\oplus$	<19.1	<19.5	<6.8	<15.6	…
Eccentricity		$0.19^{+0.09}_{-0.11}$	<0.36	0.32 ± 0.08	$0.17^{+0.11}_{-0.05}$	$0.26^{+0.27}_{-0.12}$
Semimajor axis	au	0.0578 ± 0.0018	0.0567 ± 0.0015	0.0377 ± 0.0013	0.02267 ± 0.00071	0.0228 ± 0.0016
Scaled semimajor axis (a/R_s)		30.07 ± 0.68	32.10 ± 0.62	$33.21^{+0.87}_{-0.83}$	23.95 ± 0.54	$24.0^{+1.0}_{-1.1}$
Orbital inclination	deg	$88.98^{+0.51}_{-0.17}$	89.62 ± 0.26	$88.67^{+0.14}_{-0.11}$	$89.80^{+0.14}_{-0.19}$	$89.63^{+0.27}_{-0.35}$
Equilibrium temp. ($A_{\rm Bond} = 0.0$)	K	435 ± 6	426 ± 6	384 ± 6	449 ± 7	447 ± 15
Equilibrium temp. ($A_{\rm Bond} = 0.3$)	K	398 ± 6	389 ± 5	351 ± 6	410 ± 6	…
Insolation	$F_\oplus$	$5.91^{+0.35}_{-0.33}$	$5.45^{+0.29}_{-0.27}$	$3.61^{+0.24}_{-0.22}$	$6.69^{+0.41}_{-0.36}$	$6.55^{+0.94}_{-0.80}$

Note. The reported values, uncertainties, and upper limits represent the median, 1σ lower and upper boundaries, and 2σ upper limits of the posterior probability distributions, respectively.

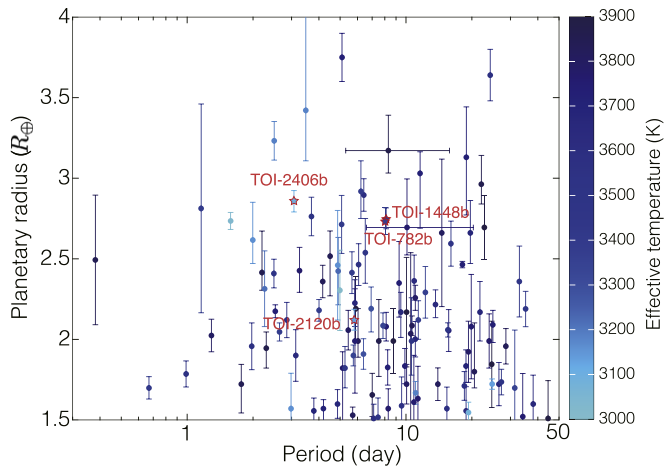

Figure 9. Radius–period relationship of planets with measured radii of 1.5–4 $R_\oplus$ and orbital periods of $\lesssim$50 days around M dwarfs with $T_{\rm eff} = 3000$–3900 K (data from http://www.exoplanet.eu). The color bar represents the effective temperature of a planet-hosting M dwarf. The four close-in, sub-Neptunes validated in this study are shown as red stars.

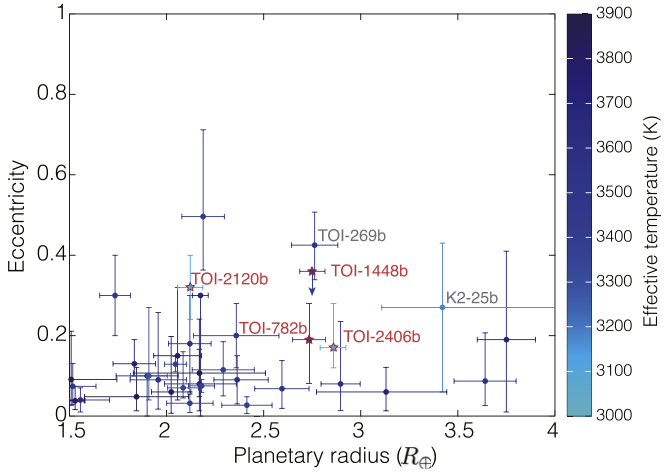

Figure 10. Eccentricity distribution of planets with measured radii of 1.5–4 $R_\oplus$ and orbital periods of $\lesssim$50 days around M dwarfs with $T_{\rm eff} = 3000$–3900 K. Only planets with measured eccentricities are shown. The color bar represents the effective temperature of a planet-hosting M dwarf. The four close-in, sub-Neptunes validated in this study are shown as red stars.

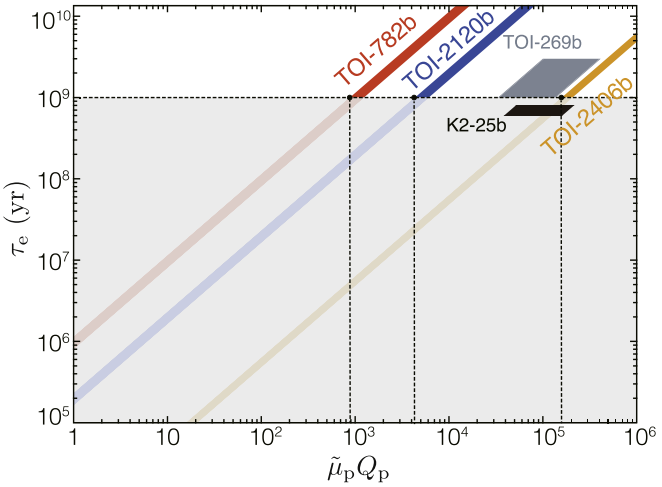

Figure 11. The eccentricity damping timescale of the three sub-Neptunes TOI-782 b (red), TOI-2120 b (blue), and TOI-2406 b (orange). We adopted the upper limit values of the planetary masses for TOI-782 b, TOI-2120 b, and TOI-2406 b. The expected tidal dissipation factors of two other eccentric sub-Neptunes, K2-25 b (black) and TOI-269 b (gray), are also shown for comparison. The vertical dashed lines correspond to $\tilde{\mu}_p Q_p$ of planets with $\tau_e = 1$ Gyr.

Acknowledgments

C.A.C. acknowledges that this research was carried out at the Jet Propulsion Laboratory, California Institute of Technology, under a contract with the National Aeronautics and Space Administration (80NM0018D0004). This work makes use of NASA Exoplanet Archive (Confirmed Planets Table; DOI:10.26133/NEA12) website and the Exoplanet Follow-up Observation Program (ExoFOP; DOI:10.26134/ExoFOP5) website, which is operated by the California Institute of Technology, under contract with the National Aeronautics and Space Administration under the Exoplanet Exploration Program and observations from the LCOGT network and the MuSCAT2-MuSCAT3 network. Part of the LCOGT telescope time was granted by NOIRLab through the Mid-Scale Innovations Program (MSIP). MSIP is funded by the NSF. The MuSCAT2 instrument at TCS operated on the island of Tenerife by the IAC in the Spanish Observatorio del Teide and the MuSCAT3 instrument at Faulkes Telescope North on Maui, HI, operated by the Las Cumbres Observatory were developed by the Astrobiology Center under financial supports by JSPS KAKENHI (18H05439) and JST PRESTO (JPMJPR1775). K.A.C. acknowledges support from the TESS mission via subaward s3449 from MIT. Funding for the TESS mission is provided by NASA's Science Mission Directorate. D.R.C. acknowledges partial support from NASA grant 18-2XRP18_2-0007. This work was partly supported by a Grant-in-Aid for Scientific Research on Innovative Areas (JSPS KAKENHI grant No. 18H05439). TRAPPIST is funded by the Belgian Fund for Scientific Research (Fond National de la Recherche Scientifique, FNRS) under the grant FRFC 2.5.594.09.F, with the participation of the Swiss National Science Foundation (SNF). I.A.S. acknowledges the support of the Ministry of Science and Higher Education of the Russian Federation under grant 075-15-2020-780 (N13.1902.21.0039). The NN-EXPLORE Exoplanet and Stellar Speckle Imager (NESSI) was funded by the NASA Exoplanet Exploration Program and the NASA Ames Research Center. NESSI was built at the Ames Research Center by Steve B. Howell, Nic Scott, Elliott P. Horch, and Emmett Quigley. Some of the observations in this paper made use of the High-Resolution Imaging instrument 'Alopeke and were obtained under Gemini LLP Proposal Number: GN/S-2021A-LP-105. 'Alopeke was funded by the NASA Exoplanet Exploration Program and built at the NASA Ames Research Center by Steve B. Howell, Nic Scott, Elliott P. Horch, and Emmett Quigley. 'Alopeke was mounted on the Gemini North telescope of the international Gemini Observatory, a program of NSF's OIR Lab, which is managed by the Association of Universities for Research in Astronomy (AURA) under a cooperative agreement with the National Science Foundation on behalf of the Gemini partnership: the National Science Foundation (United States), National Research Council (Canada), Agencia Nacional de Investigación y Desarrollo (Chile), Ministerio de Ciencia, Tecnología e Innovación (Argentina), Ministério da Ciência, Tecnologia, Inovações e Comunicações (Brazil), and the Korea Astronomy and Space Science Institute (Republic of Korea). J.K. gratefully acknowledges the support of the Swedish National Space Agency (SNSA; DNR 2020-00104) and of the Swedish Research Council (VR: Etableringsbidrag 2017-04945. G.M. has received funding from the Ariel Post-doctoral Fellowship program of the Swedish National Space Agency (SNSA). M.T. is supported by JSPS KAKENHI grant No.18H05442. R.L. acknowledges funding from University of La Laguna through the Margarita Salas Fellowship from the Spanish Ministry of Universities ref. UNI/551/2021 May 26, and under the EU Next Generation funds. W.W. was supported by the National Science Foundation Graduate Research Fellowship Program under grant No. DGE-1650115. Resources supporting this work were provided by the NASA High-End Computing (HEC) Program through the NASA Advanced Supercomputing (NAS) Division at Ames Research Center for the production of the SPOC data products. We acknowledge the use of public TESS data from pipelines at the TESS Science Office and at the TESS Science Processing Operations Center. The research leading to these results has received funding from the ARC grant for Concerted Research Actions, financed by the Wallonia-Brussels Federation. TRAPPIST is funded by the Belgian Fund for Scientific Research (Fond National de la Recherche Scientifique, FNRS) under the grant PDR T.0120.21. TRAPPIST-North is a project funded by the University of Liege (Belgium), in collaboration with Cadi Ayyad University of Marrakech (Morocco). M.G. is F.R.S.-FNRS Research Director and E.J. is F.R.S.-FNRS Senior Research Associate. The postdoctoral fellowship of K.B. is funded by F.R.S.-FNRS grant T.0109.20 and by the Francqui Foundation. F.J.P. acknowledges financial support from the grant CEX2021-001131-S funded by MCIN/AEI/10.13039/501100011033. This publication benefits from the support of the French Community of Belgium in the context of the FRIA Doctoral Grant awarded to M.T. We thank the anonymous referee for valuable comments and suggestions that improved our manuscript. This research is based in part on data collected at the Subaru Telescope, which is operated by the National Astronomical Observatory of Japan. We are honored and grateful for the opportunity of observing the Universe from Maunakea, which has the cultural, historical, and natural significance in Hawaii.

Facility: TESS, Subaru (IRD), Sanchez (MuSCAT2), FTN (MuSCAT3), SSO:1 m (Sinistro), Keck:II (NIRC2), Gemini: Gillett (NIRI, 'Alopeke), SOAR (HRCam), LDT (DSSI), Hale (PHARO), WIYN (NESSI), HATSouth, Gaia, FLWO:2MASS, and WISE.

Appendix A
Spectral Energy Distributions

The SEDs of the four host stars are shown in Figure 12.

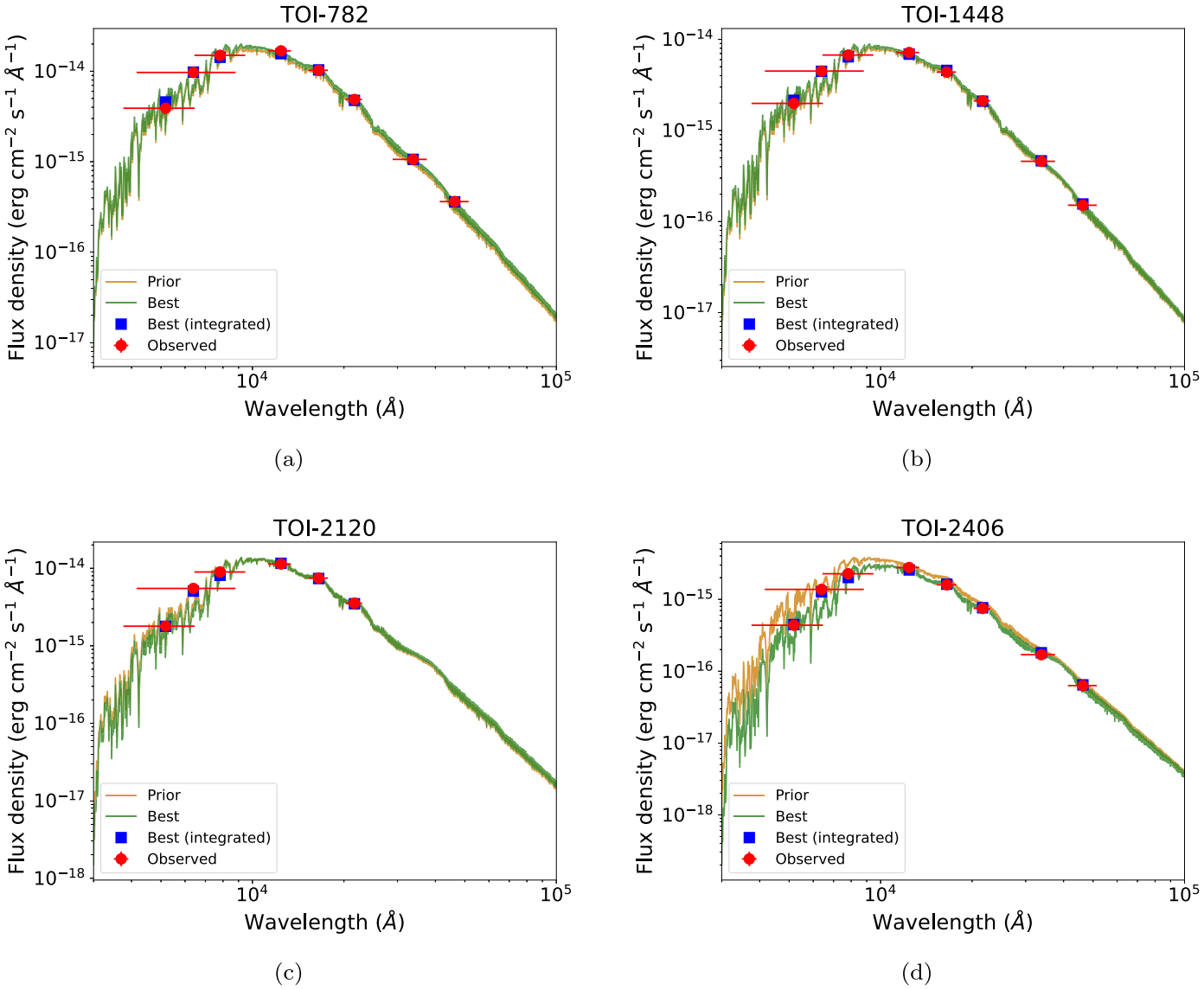

Figure 12. (a) SED of TOI-782. Panels (b), (c), and (d) are the same as (a), but for TOI-1448, TOI-2120, and TOI-2406, respectively. Yellow and blue curves show the prior and posterior SED models. Red diamonds and blue squares are observational data and best-fit results, respectively.

Appendix B
TESS Light Curves of the Individual Sectors

The TESS PDC-SAP light curves of each sector for TOI-782, TOI-1448, TOI-2120, and TOI-2406 are shown from Figures 13–16.

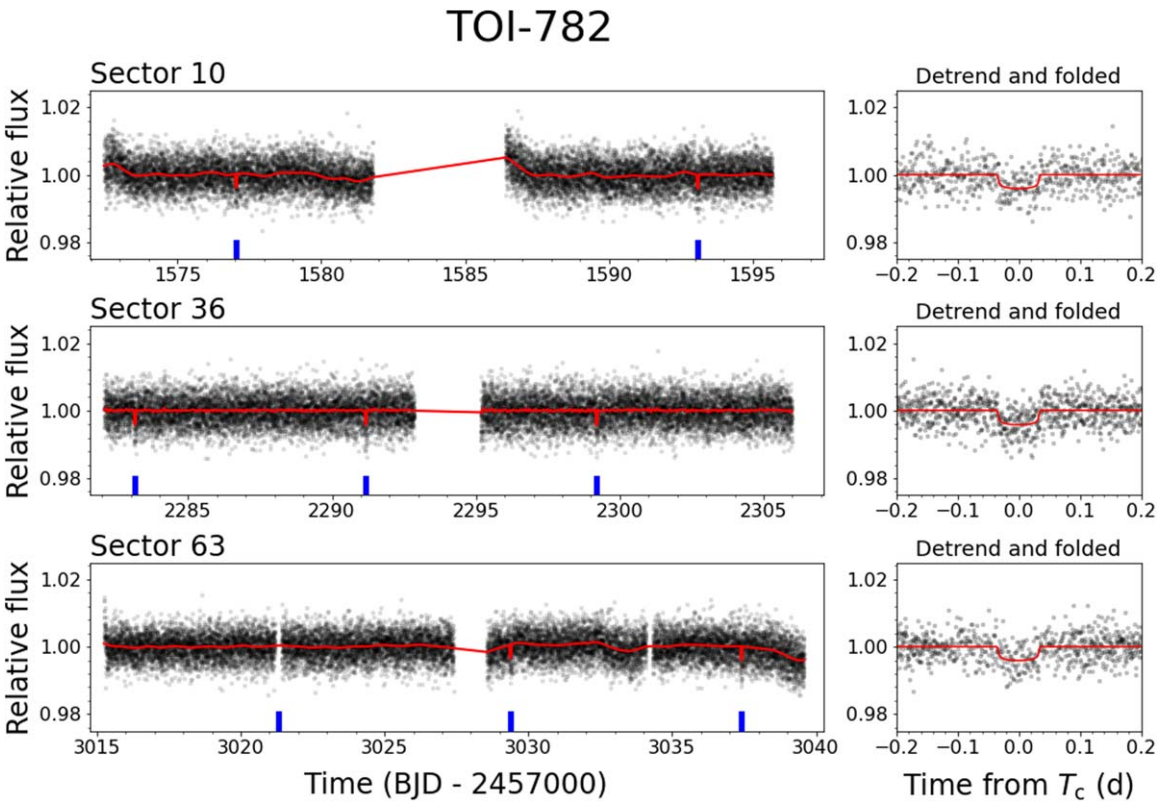

Figure 13. Left: TESS PDC-SAP light curves of TOI-782. Black dots and red lines are undetrended data points and maximum-likelihood transit + GP models, respectively. The locations of the transits covered by TESS are marked by blue vertical lines. Right: same as left but the data are detrended and phase folded by the orbital period of TOI-782 b for each sector.

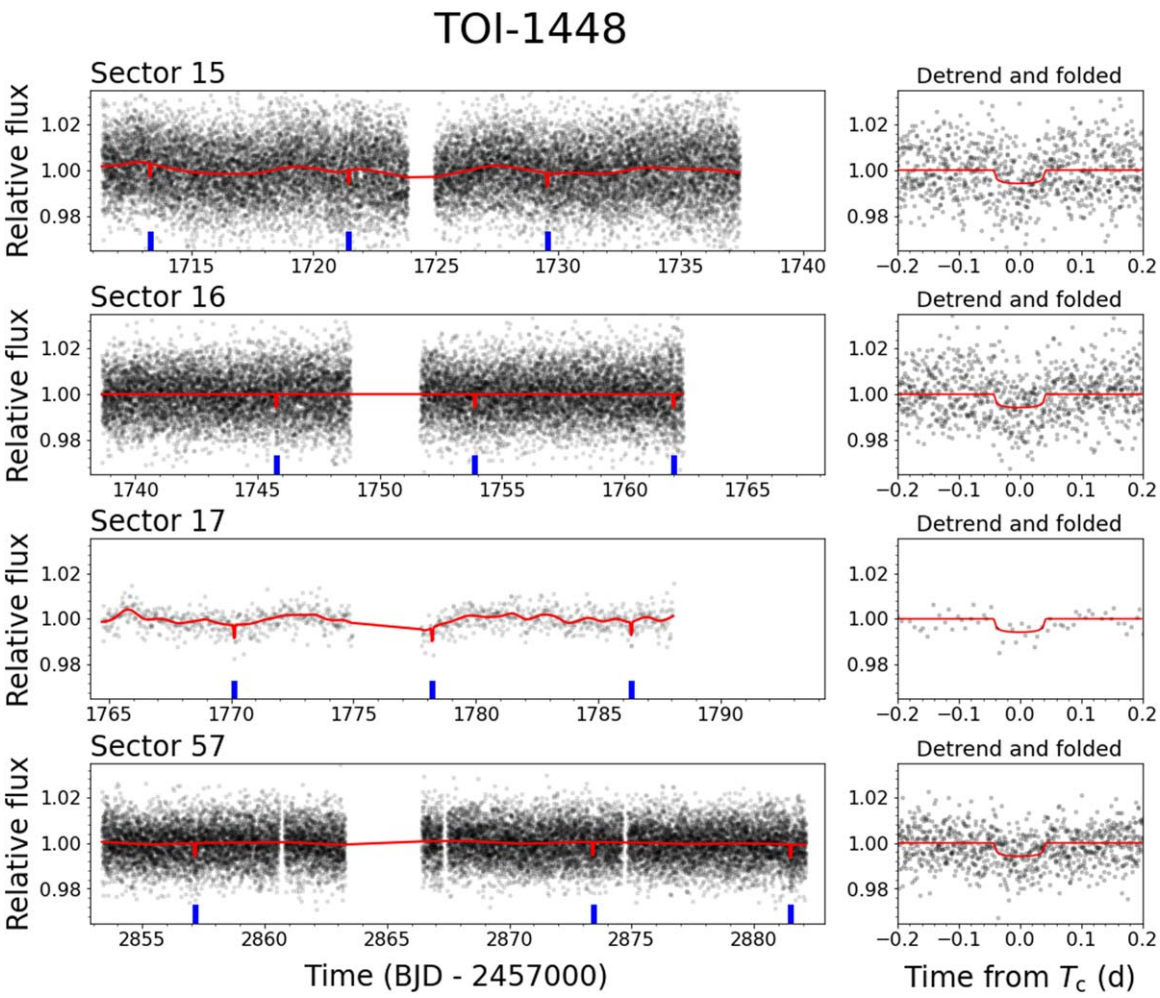

Figure 14. Same as Figure 13, but for TOI-1448.

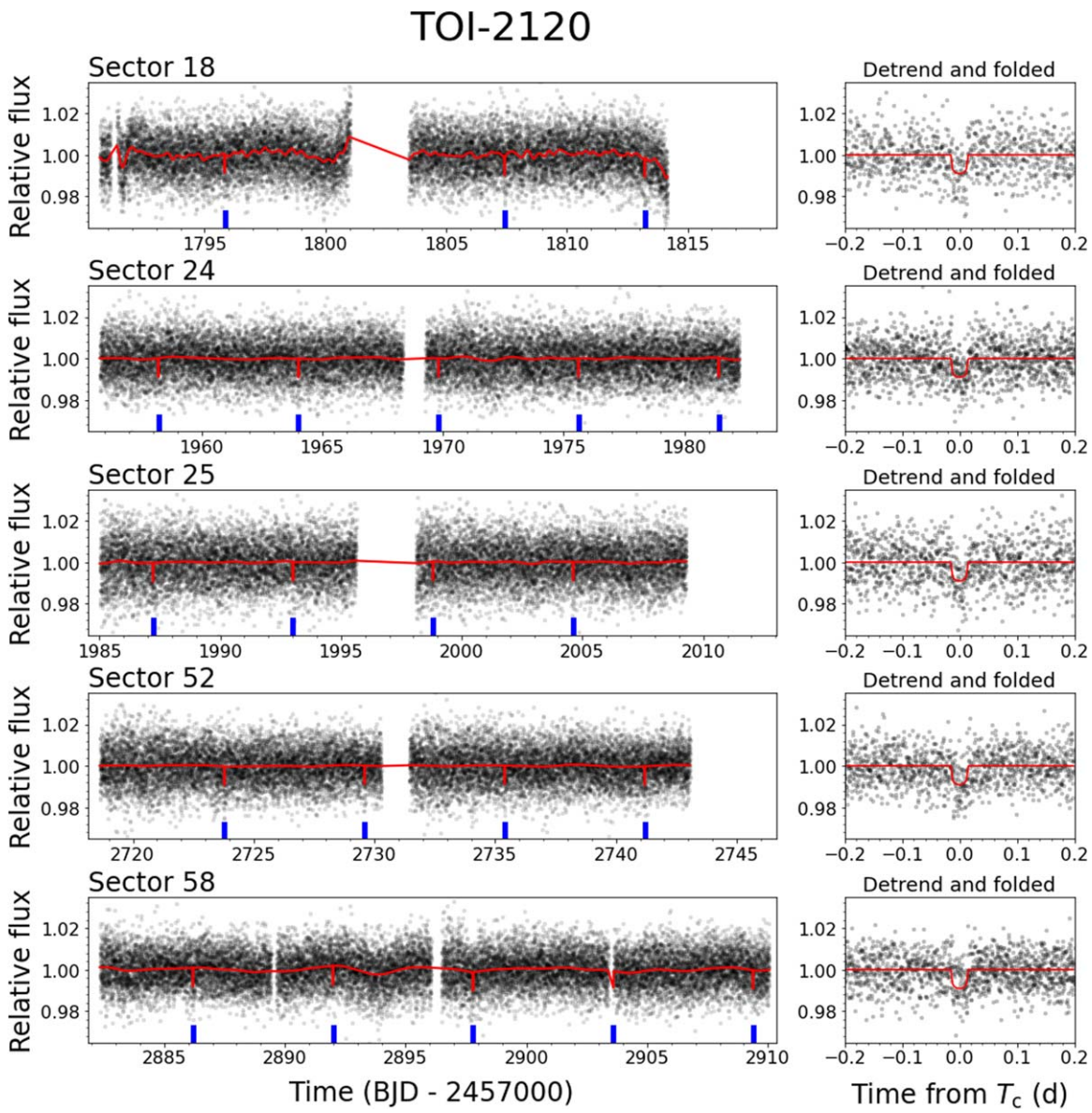

Figure 15. Same as Figure 13, but for TOI-2120.

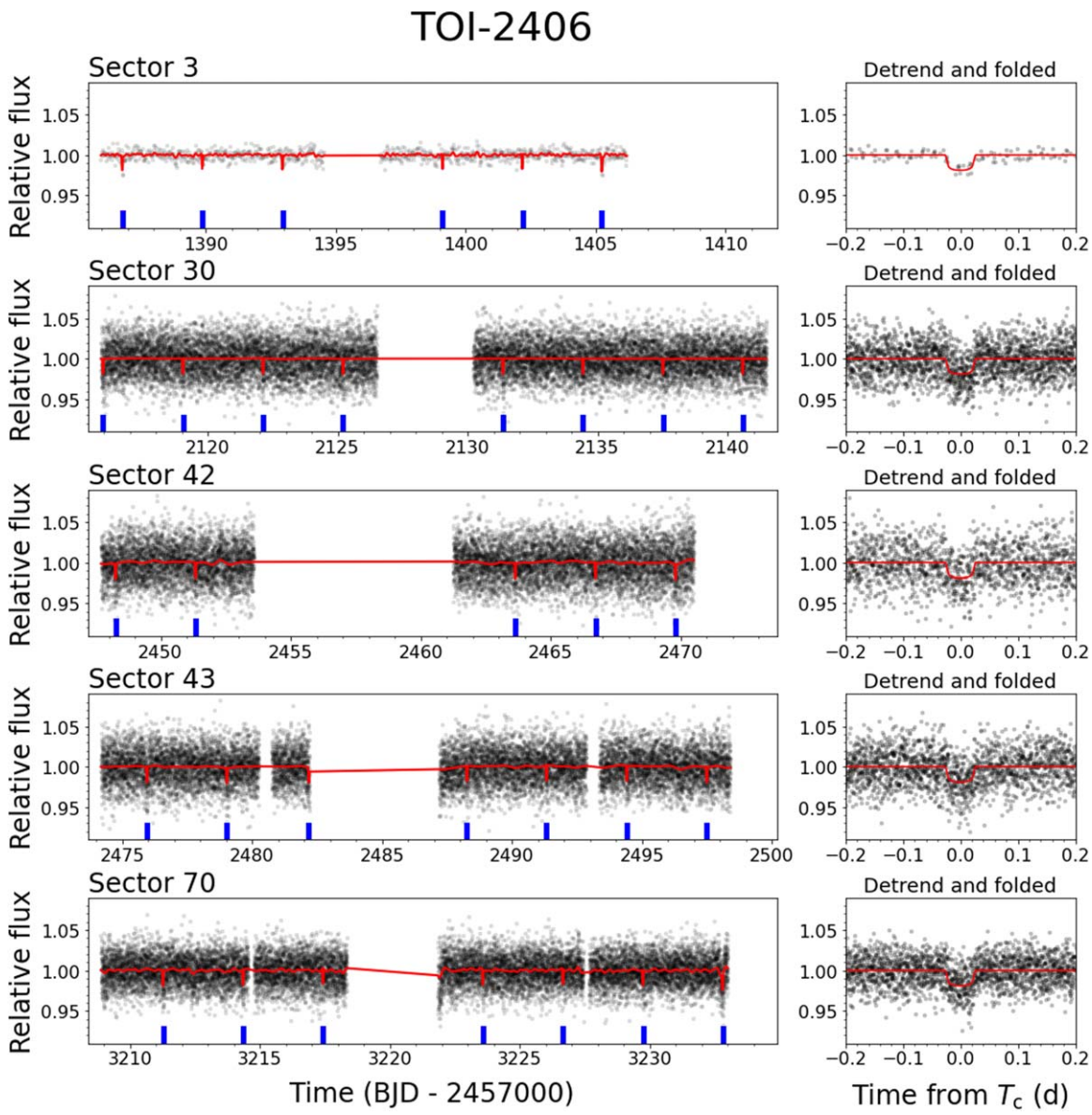

Figure 16. Same as Figure 13, but for TOI-2406.

Appendix C
Individual Transit Light Curves from Ground-based Observations

The individual transit light curves of the four planets obtained with the ground-based instruments are shown in Figure 17.

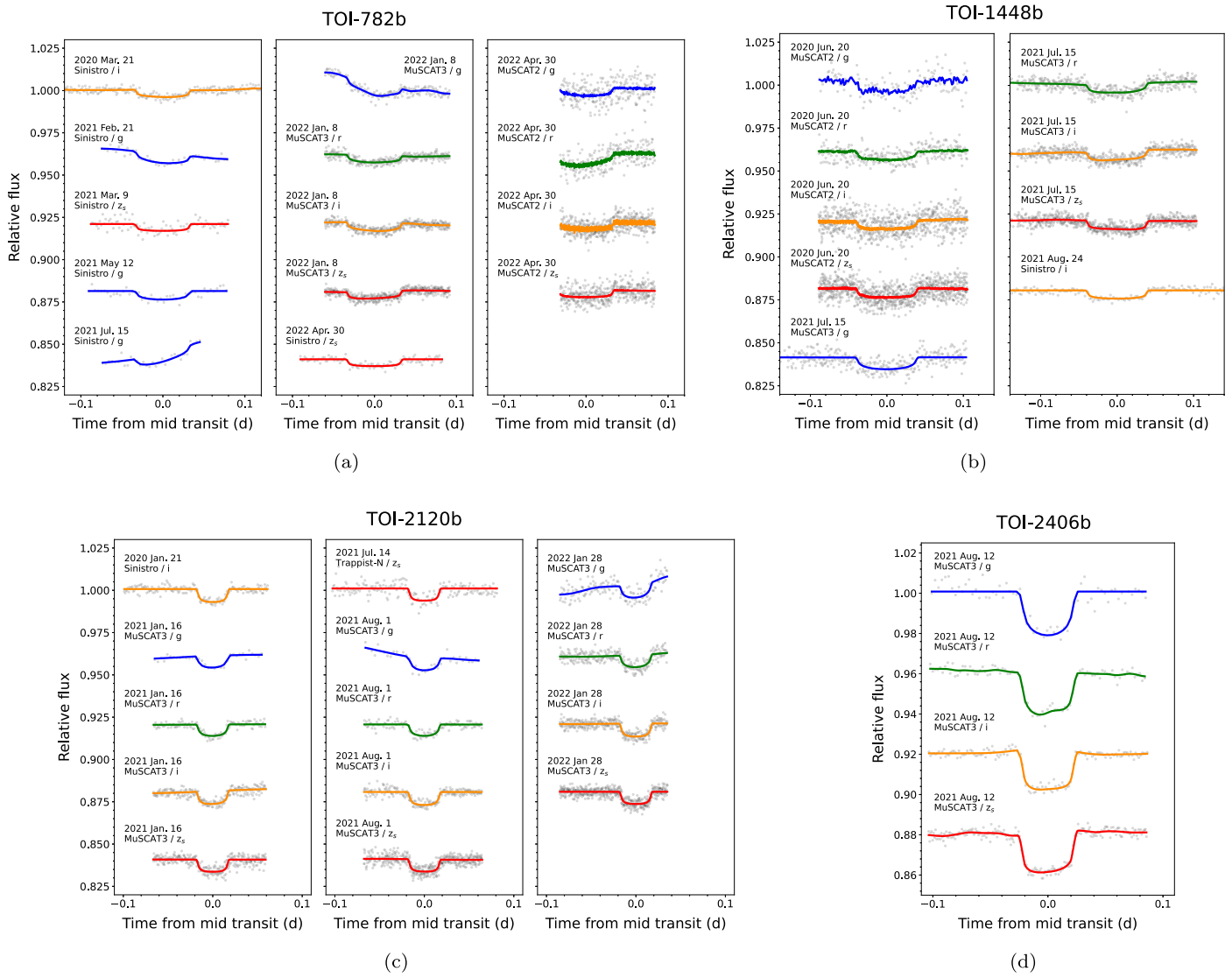

Figure 17. (a) Individual transit light curves of TOI-782 b obtained with ground-based telescopes. Panels (b), (c), and (d) are the same as (a), but for TOI-1448 b, TOI-2120 b, and TOI-2406 b, respectively.

ORCID iDs

Yasunori Hori https://orcid.org/0000-0003-4676-0251
Akihiko Fukui https://orcid.org/0000-0002-4909-5763
Teruyuki Hirano https://orcid.org/0000-0003-3618-7535
Norio Narita https://orcid.org/0000-0001-8511-2981
Jerome P. de Leon https://orcid.org/0000-0002-6424-3410
Hiroyuki Tako Ishikawa https://orcid.org/0000-0001-6309-4380
Joel D. Hartman https://orcid.org/0000-0001-8732-6166
Giuseppe Morello https://orcid.org/0000-0002-4262-5661
Nestor Abreu García https://orcid.org/0009-0002-5067-5463
Víctor J. S. Béjar https://orcid.org/0000-0002-5086-4232
Ilaria Carleo https://orcid.org/0000-0002-0810-3747
Gareb Enoc https://orcid.org/0000-0003-0597-7809
Emma Esparza-Borges https://orcid.org/0000-0002-2341-3233
Izuru Fukuda https://orcid.org/0000-0002-9436-2891
Daniel Galán https://orcid.org/0000-0001-6191-8251
Yuya Hayashi https://orcid.org/0000-0001-8877-0242
Masahiro Ikoma https://orcid.org/0000-0002-5658-5971
Kai Ikuta https://orcid.org/0000-0002-5978-057X
Keisuke Isogai https://orcid.org/0000-0002-6480-3799
Taiki Kagetani https://orcid.org/0000-0002-5331-6637
Yugo Kawai https://orcid.org/0000-0002-0488-6297
Kiyoe Kawauchi https://orcid.org/0000-0003-1205-5108
Tadahiro Kimura https://orcid.org/0000-0001-8477-2523
Takanori Kodama https://orcid.org/0000-0001-9032-5826
Judith Korth https://orcid.org/0000-0002-0076-6239
Nobuhiko Kusakabe https://orcid.org/0000-0001-9194-1268
Andrés Laza-Ramos https://orcid.org/0000-0003-3316-3044
John H. Livingston https://orcid.org/0000-0002-4881-3620
Rafael Luque https://orcid.org/0000-0002-4671-2957
Kohei Miyakawa https://orcid.org/0000-0002-5706-3497
Mayuko Mori https://orcid.org/0000-0003-1368-6593
Felipe Murgas https://orcid.org/0000-0001-9087-1245
Jaume Orell-Miquel https://orcid.org/0000-0003-2066-8959
Enric Palle https://orcid.org/0000-0003-0987-1593
Hannu Parviainen https://orcid.org/0000-0001-5519-1391
Alberto Peláez-Torres https://orcid.org/0000-0001-9204-8498
Marta Puig-Subirà https://orcid.org/0000-0001-8955-7574
Manuel Sánchez-Benavente https://orcid.org/0000-0003-2693-279X
Monika Stangret https://orcid.org/0000-0002-1812-8024
Yuka Terada https://orcid.org/0000-0003-2887-6381
Sara Muñoz Torres https://orcid.org/0000-0003-4269-4779
Noriharu Watanabe https://orcid.org/0000-0002-7522-8195
Gaspar Á. Bakos https://orcid.org/0000-0001-7204-6727
Khalid Barkaoui https://orcid.org/0000-0003-1464-9276
Charles Beichman https://orcid.org/0000-0002-5627-5471
Zouhair Benkhaldoun https://orcid.org/0000-0001-6285-9847
Andrew W. Boyle https://orcid.org/0000-0001-6037-2971
David R. Ciardi https://orcid.org/0000-0002-5741-3047
Catherine A. Clark https://orcid.org/0000-0002-2361-5812
Karen A. Collins https://orcid.org/0000-0001-6588-9574
Kevin I. Collins https://orcid.org/0000-0003-2781-3207
Dennis M. Conti https://orcid.org/0000-0003-2239-0567
Ian J.M. Crossfield https://orcid.org/0000-0002-1835-1891
Mark E. Everett https://orcid.org/0000-0002-0885-7215
Elise Furlan https://orcid.org/0000-0001-9800-6248
Mourad Ghachoui https://orcid.org/0000-0003-3986-0297
Michaël Gillon https://orcid.org/0000-0003-1462-7739
Erica J. Gonzales https://orcid.org/0000-0002-9329-2190
Jesus Higuera https://orcid.org/0000-0002-3985-8528
Keith Horne https://orcid.org/0000-0003-1728-0304
Steve B. Howell https://orcid.org/0000-0002-2532-2853
Emmanuël Jehin https://orcid.org/0000-0001-8923-488X
Kathryn V. Lester https://orcid.org/0000-0002-9903-9911
Michael B. Lund https://orcid.org/0000-0003-2527-1598
Rachel Matson https://orcid.org/0000-0001-7233-7508
Elisabeth C. Matthews https://orcid.org/0000-0003-0593-1560
Francisco J. Pozuelos https://orcid.org/0000-0003-1572-7707
Boris S. Safonov https://orcid.org/0000-0003-1713-3208
Joshua E. Schlieder https://orcid.org/0000-0001-5347-7062
Richard P. Schwarz https://orcid.org/0000-0001-8227-1020
Ramotholo Sefako https://orcid.org/0000-0003-3904-6754
Ivan A. Strakhov https://orcid.org/0000-0003-0647-6133
Mathilde Timmermans https://orcid.org/0009-0008-2214-5039
William C. Waalkes https://orcid.org/0000-0002-8961-0352
Carl Ziegler https://orcid.org/0000-0002-0619-7639
David Charbonneau https://orcid.org/0000-0002-9003-484X
Zahra Essack https://orcid.org/0000-0002-2482-0180
Natalia M. Guerrero https://orcid.org/0000-0002-5169-9427
Hiroki Harakawa https://orcid.org/0000-0002-7972-0216
Christina Hedges https://orcid.org/0000-0002-3385-8391
Masato Ishizuka https://orcid.org/0000-0003-1906-4525
Jon M. Jenkins https://orcid.org/0000-0002-4715-9460
Mihoko Konishi https://orcid.org/0000-0003-0114-0542
Takayuki Kotani https://orcid.org/0000-0001-6181-3142
Tomoyuki Kudo https://orcid.org/0000-0002-9294-1793
Masayuki Kuzuhara https://orcid.org/0000-0002-4677-9182
Jun Nishikawa https://orcid.org/0000-0001-9326-8134
Masashi Omiya https://orcid.org/0000-0002-5051-6027
George R. Ricker https://orcid.org/0000-0003-2058-6662
Sara Seager https://orcid.org/0000-0002-6892-6948
Stephanie Striegel https://orcid.org/0009-0008-5145-0446
Motohide Tamura https://orcid.org/0000-0002-6510-0681
Roland Vanderspek https://orcid.org/0000-0001-6763-6562
Sébastien Vievard https://orcid.org/0000-0003-4018-2569
Joshua N. Winn https://orcid.org/0000-0002-4265-047X

References

Allard, F., Homeier, D., & Freytag, B. 2011, in ASP Conf. Ser. 448, XVI Cambridge Workshop on Cool Stars, Stellar Systems, and the Sun, ed. C. Johns-Krull, M. K. Browning, & A. A. West (San Francisco, CA: ASP), 91, Allard
Anderson, O. L., Dubrovinsky, L., Saxena, S. K., et al. 2001, GeoRL, 28, 399
Barkaoui, K., Burdanov, A., Hellier, C., et al. 2019, AJ, 157, 43
Belokurov, V., Penoyre, Z., Oh, S., et al. 2020, MNRAS, 496, 1922
Benneke, B., Roy, P.-A., Coulombe, L.-P., et al. 2024, arXiv:2403.03325
Bensby, T., Feltzing, S., & Oey, M. S. 2014, A&A, 562, A71
Berger, T. A., Huber, D., Gaidos, E., et al. 2020, AJ, 160, 108
Bergsten, G. J., Pascucci, I., Mulders, G. D., et al. 2022, AJ, 164, 190
Bonfils, X., Delfosse, X., Udry, S., et al. 2013, A&A, 549, A109

Bouma, L. G., Hartman, J. D., Brahm, R., et al. 2020, AJ, 160, 239
Brown, T. M., Baliber, N., Bianco, F. B., et al. 2013, PASP, 125, 1031
Burn, R., Schlecker, M., Mordasini, C., et al. 2021, A&A, 656, A72
Burrows, A., Heng, K., & Nampaisarn, T. 2011, ApJ, 736, 47
Caldwell, D. A., Tenenbaum, P., Twicken, J. D., et al. 2020, RNAAS, 4, 201
Chambers, K. C., Magnier, E. A., Metcalfe, N., et al. 2016, arXiv:1612.05560
Clark, C. A., van Belle, G. T., Ciardi, D. R., et al. 2022, AJ, 163, 232
Clausen, N., & Tilgner, A. 2015, A&A, 584, A60
Cloutier, R., & Menou, K. 2020, AJ, 159, 211
Cointepas, M., Almenara, J. M., Bonfils, X., et al. 2021, A&A, 650, A145
Collins, K. 2019, AAS Meeting Abstracts, 223, 140.05
Collins, K. A., Kielkopf, J. F., Stassun, K. G., et al. 2017, AJ, 153, 77
Bakos, G. Á., Csubry, Z., Penev, K., et al. 2013, PASP, 125, 154
Dekany, R., Roberts, J., Burruss, R., et al. 2013, ApJ, 776, 130
Donati, J. F., Kouach, D., Moutou, C., et al. 2020, MNRAS, 498, 5684
Dorn, R. J., Follert, R., Bristow, P., et al. 2016, Proc. SPIE, 9908, 99080I
Dressing, C. D., & Charbonneau, D. 2013, ApJ, 767, 95
Dressing, C. D., & Charbonneau, D. 2015, ApJ, 807, 45
Edelson, R. A., & Krolik, J. H. 1988, ApJ, 333, 646
Efroimsky, M. 2012, ApJ, 746, 150
Fabrycky, D., & Tremaine, S. 2007, ApJ, 669, 1298
Foreman-Mackey, D., Agol, E., Ambikasaran, S., et al. 2017, AJ, 154, 220
Foreman-Mackey, D., Hogg, D. W., Lang, D., et al. 2013, PASP, 125, 306
Fukui, A., Narita, N., Tristram, P. J., et al. 2011, PASJ, 63, 287
Fulton, B. J., & Petigura, E. A. 2018, AJ, 156, 264
Gagné, J., Mamajek, E. E., Malo, L., et al. 2018, ApJ, 856, 23
Gaia Collaboration, Prusti, T., de Bruijne, J. H. J., et al. 2016, A&A, 595, A1
Gaia Collaboration, Vallenari, A., Brown, A. G. A., et al. 2023, A&A, 674, A1
Garcia, L. J., Timmermans, M., Pozuelos, F. J., et al. 2022, MNRAS, 509, 4817
Giacalone, S., Dressing, C. D., Jensen, E. L. N., et al. 2021, AJ, 161, 24
Giacalone, S., Dressing, C. D., Jensen, E. L. N., et al. 2021, AJ, 161, 24
Gibson, R. K., Oppenheimer, R., Matthews, C. T., et al. 2020, JATIS, 6, 011002
Gillon, M., Anderson, D. R., Collier-Cameron, A., et al. 2013, A&A, 552, A82
Gillon, M., Triaud, A. H. M. J., Demory, B.-O., et al. 2017, Natur, 542, 456
Ginzburg, S., Schlichting, H. E., & Sari, R. 2016, ApJ, 825, 29
Ginzburg, S., Schlichting, H. E., & Sari, R. 2018, MNRAS, 476, 759
Girardi, L., Groenewegen, M. A. T., Hatziminaoglou, E., et al. 2005, A&A, 436, 895
Green, G. M., Schlafly, E., Zucker, C., et al. 2019, ApJ, 887, 93
Guerrero, N. M., Seager, S., Huang, C. X., et al. 2021, ApJS, 254, 39
Gupta, A., Nicholson, L., & Schlichting, H. E. 2022, MNRAS, 516, 4585
Gupta, A., & Schlichting, H. E. 2019, MNRAS, 487, 24
Haldemann, J., Alibert, Y., Mordasini, C., et al. 2020, A&A, 643, A105
Hansen, B. M. S., & Murray, N. 2015, MNRAS, 448, 1044
Hardegree-Ullman, K. K., Cushing, M. C., Muirhead, P. S., et al. 2019, AJ, 158, 75
Hayward, T. L., Brandl, B., Pirger, B., et al. 2001, PASP, 113, 105
Hirano, T., Dai, F., Gandolfi, D., et al. 2018, AJ, 155, 127
Hirano, T., Kuzuhara, M., Kotani, T., et al. 2020, PASJ, 72, 93
Hodapp, K. W., Jensen, J. B., Irwin, E. M., et al. 2003, PASP, 115, 1388
Holmberg, M., & Madhusudhan, N. 2024, A&A, 683, L2
Horch, E. P., Veillette, D. R., Baena Gallé, R., et al. 2009, AJ, 137, 5057
Hsu, D. C., Ford, E. B., & Terrien, R. 2020, MNRAS, 498, 2249
Ikoma, M., & Hori, Y. 2012, ApJ, 753, 66
Ishikawa, H. T., Aoki, W., Hirano, T., et al. 2022, AJ, 163, 72
Ishikawa, H. T., Aoki, W., Kotani, T., et al. 2020, PASJ, 72, 102
Jehin, E., Gillon, M., Queloz, D., et al. 2011, Msngr, 145, 2
Jenkins, J. M., Chandrasekaran, H., McCauliff, S. D., et al. 2010, Proc. SPIE, 7740, 77400D
Jenkins, J. M., Twicken, J. D., McCauliff, S., et al. 2016, Proc. SPIE, 9913, 99133E
Jensen, E., 2013 Tapir: A web interface for transit/eclipse observability, Astrophysics Source Code Library, ascl:1306.007
Karki, B. B., Wentzcovitch, R. M., de Gironcoli, S., et al. 2000, PhRvB, 62, 14750
Kipping, D. M. 2014, MNRAS, 444, 2263
Kotani, T., Tamura, M., Nishikawa, J., et al. 2018, Proc. SPIE, 10702, 1070211
Kovács, G., Bakos, G., & Noyes, R. W. 2005, MNRAS, 356, 557
Kurokawa, H., & Tanigawa, T. 2018, MNRAS, 479, 635
Kuwahara, A., Kurokawa, H., & Ida, S. 2019, A&A, 623, A179
Kuzuhara, M., Hirano, T., Kotani, T., et al. 2018, Proc. SPIE, 10702, 1070260
Lee, E. J., Chiang, E., & Ormel, C. W. 2014, ApJ, 797, 95
Limbach, M. A., & Turner, E. L. 2015, PNAS, 112, 20
Lopez, E. D., & Fortney, J. J. 2013, ApJ, 776, 2
Luque, R., & Pallé, E. 2022, Sci, 377, 1211
Madhusudhan, N., Sarkar, S., Constantinou, S., et al. 2023, ApJL, 956, L13
Mahadevan, S., Anderson, T., Balderrama, E., et al. 2018, Proc. SPIE, 10702, 1070214
Mainzer, A., Bauer, J., Grav, T., et al. 2011, ApJ, 731, 53
Maldonado, J., Micela, G., Baratella, M., et al. 2020, A&A, 644, A68
Mandel, K., & Agol, E. 2002, ApJ, 580, L171
Mann, A. W., Dupuy, T., Kraus, A. L., et al. 2019, ApJ, 871, 63
Mann, A. W., Feiden, G. A., Gaidos, E., et al. 2015, ApJ, 804, 64
Mann, A. W., Gaidos, E., Mace, G. N., et al. 2016, ApJ, 818, 46
Martinez, C. F., Cunha, K., Ghezzi, L., et al. 2019, ApJ, 875, 29
McCully, C., Volgenau, N. H., Harbeck, D.-R., et al. 2018, Proc. SPIE, 10707, 107070K
Mori, M., Livingston, J. H., Leon, J. d., et al. 2022, AJ, 163, 298
Mulders, G. D., Pascucci, I., & Apai, D. 2015, ApJ, 798, 112
Murray, C. D., & Dermott, S. F. 1999, Solar System Dynamics (Cambridge: Cambridge Univ. Press)
Narita, N., Fukui, A., Kusakabe, N., et al. 2019, JATIS, 5, 015001
Narita, N., Fukui, A., Yamamuro, T., et al. 2020, Proc. SPIE, 11447, 114475K
Ngo, H., Knutson, H. A., Hinkley, S., et al. 2016, ApJ, 827, 8
Ormel, C. W., Shi, J.-M., & Kuiper, R. 2015, MNRAS, 447, 3512
Owen, J. E., & Wu, Y. 2013, ApJ, 775, 105
Owen, J. E., & Wu, Y. 2017, ApJ, 847, 29
Parviainen, H. 2015, MNRAS, 450, 3233
Parviainen, H., & Aigrain, S. 2015, MNRAS, 453, 3821
Petigura, E. A., Rogers, J. G., Isaacson, H., et al. 2022, AJ, 163, 179
Quirrenbach, A., Amado, P. J., Caballero, J. A., et al. 2014, Proc. SPIE, 9147, 91471F
Ricker, G. R., Winn, J. N., Vanderspek, R., et al. 2015, JATIS, 1, 014003
Rodriguez, D. 2016, dr-rodriguez/Kinematics-App: Stellar Kinematics v1.0, Zenodo, doi:10.5281/zenodo.192159
Rogers, L. A. 2015, ApJ, 801, 41
Sabotta, S., Schlecker, M., Chaturvedi, P., et al. 2021, A&A, 653, A114
Safonov, B. S., Lysenko, P. A., & Dodin, A. V. 2017, AstL, 43, 344
Salpeter, E. E., & Zapolsky, H. S. 1967, PhRv, 158, 876
Sandoval, A., Contardo, G., & David, T. J. 2021, ApJ, 911, 117
Scott, N. J., Howell, S. B., Gnilka, C. L., et al. 2021, FrASS, 8, 138
Scott, N. J., Howell, S. B., Horch, E. P., et al. 2018, PASP, 130, 054502
Seager, S., Kuchner, M., Hier-Majumder, C. A., et al. 2007, ApJ, 669, 1279
Seifahrt, A., Stürmer, J., Bean, J. L., et al. 2018, Proc. SPIE, 10702, 107026D
Skrutskie, M. F., Cutri, R. M., Stiening, R., et al. 2006, AJ, 131, 1163
Smith, J. C., Stumpe, M. C., Van Cleve, J. E., et al. 2012, PASP, 124, 1000
Stefansson, G., Mahadevan, S., Maney, M., et al. 2020, AJ, 160, 192
Stumpe, M. C., Smith, J. C., Catanzarite, J. H., et al. 2014, PASP, 126, 100
Stumpe, M. C., Smith, J. C., Van Cleve, J. E., et al. 2012, PASP, 124, 985
Tamura, M., Suto, H., Nishikawa, J., et al. 2012, Proc. SPIE, 8446, 84461T
Tokovinin, A., Mason, B. D., & Hartkopf, W. I. 2010, AJ, 139, 743
Tuomi, M., Jones, H. R. A., Barnes, J. R., et al. 2014, MNRAS, 441, 1545
Twicken, J. D., Catanzarite, J. H., Clarke, B. D., et al. 2018, PASP, 130, 064502
Van Eylen, V., Agentoft, C., Lundkvist, M. S., et al. 2018, MNRAS, 479, 4786
Van Eylen, V., Albrecht, S., Huang, X., et al. 2019, AJ, 157, 61
Venturini, J., Guilera, O. M., Haldemann, J., et al. 2020, A&A, 643, L1
Wang, J., & Ford, E. B. 2011, MNRAS, 418, 1822
Weidenschilling, S. J., & Marzari, F. 1996, Natur, 384, 619
Weiss, L. M., & Marcy, G. W. 2014, ApJL, 783, L6
Wells, R. D., Rackham, B. V., Schanche, N., et al. 2021, A&A, 653, A97
Wildi, F., Blind, N., Reshetov, V., et al. 2017, Proc. SPIE, 10400, 1040018
Winters, J. G., Charbonneau, D., Henry, T. J., et al. 2021, AJ, 161, 63
Winters, J. G., Henry, T. J., Jao, W.-C., et al. 2019, AJ, 157, 216
Wizinowich, P., Acton, D. S., Shelton, C., et al. 2000, PASP, 112, 315
Wright, E. L., Eisenhardt, P. R. M., Mainzer, A. K., et al. 2010, AJ, 140, 1868
Zechmeister, M., Dreizler, S., Ribas, I., et al. 2019, A&A, 627, A49
Zechmeister, M., & Kürster, M. 2009, A&A, 496, 577
Zeng, L., & Sasselov, D. 2013, PASP, 125, 227